Dye Sensitization in a Photoelectrochemical Water-Splitting Cell Using N,N'-Bis(3-phosphonopropyl)-3,4,9,10-perylenedicarboximide

by

Andrew James Emig

Submitted in Partial Fulfillment of the Requirements

for the Degree of

Master of Science

in the

Chemistry

Program

YOUNGSTOWN STATE UNIVERSITY

August, 2012

Dye Sensitization in a Photoelectrochemical Water-Splitting Cell Using N,N'-Bis(3-phosphonopropyl)-3,4,9,10-perylenedicarboximide

Andrew James Emig

I hereby release this thesis to the public. I understand that this thesis will be made available from the OhioLINK ETD Center and the Maag Library Circulation Desk for public access. I also authorize the University or other individuals to make copies of this thesis as needed for scholarly research.

Signature:

Andrew J. Emig, Student Date

Approvals:

Clovis A. Linkous, Ph.D., Thesis Advisor Date

Sherri R. Lovelace-Cameron, Ph.D., Committee Member Date

Howard D. Mettee, Ph.D., Committee Member Date

Peter J. Kasvinsky, Dean of School of Graduate Studies and Research Date

ABSTRACT

Enhanced surface area thin film titania electrodes were prepared by spin coating of a titania sol onto fluorine tin oxide substrates. The electrodes were characterized by profilometry, scanning electron microscopy, and ultraviolet-visible light spectrometry. Capacitance measurements were used to assess surface area enhancement. The propylphosphonic acid derivative of perylene diimide was synthesized for use in sensitization of the titania films. Complete purification of the crude product was complicated due to the low solubility of the dye derivative. Nonetheless, mass spectrometry, gel electrophoresis, nuclear magnetic resonance, infrared spectrometry, and elemental analysis were carried out to characterize the product. Electrochemical measurements were used to study the efficacy of the dye as a titania sensitizer. The results indicate the perylene derivative is energetically capable of water oxidation. However, charge transfer from the dye into the titania layer was not seen. It is believed this is due to an energy band mismatch between the reduction potential of the dye and the conduction band of the titania layer.

TABLE OF CONTENTS

LIST OF TABLES

LIST OF FIGURES

ACKNOWLEDGEMENTS

There are a number of people for whose help I am very grateful. First, I want to thank my family & friends for their support of my studies. A big thank you goes out to John Dodson & Bob Schmidt in the machine shop at YSU for their excellent work machining the electrochemical cell to my specifications. I want to thank Dr. Tom Oder of the Physics Department for the use of equipment and lab space.

I am grateful for a number of our faculty and staff in the Chemistry Department for their expertise and willingness to assist me throughout my studies. Dr. Dingqiang Li supervised and instructed me on the use of the electron microscope; Dr. Ganesaratnam Balendiran kindly obliged to run the gel electrophoresis experiment for me; Ray Hoff lent his time and knowledge to me when it came time for mass-spec measurements and assisted me in manipulating the IR software; many thanks to Dr. Mattias Zeller for much useful commentary on my experimental results and my writing. Dr. Zeller also helped me work through the solid ^{13}C NMR data and led me in a couple unsuccessful attempts to grow crystals of the perylene derivative. I'd like to thank all of the "Organicers" in the department for their time and patience while I was trying to work up and purify the crude product of the dye synthesis; this includes but is not limited to Dr. 'No' - Peter Norris, Dr. 'J' – John Jackson, Isaac Mills, and Olumuyiwa 'M. J.' Adesoye.

I want to extend a warm thanks to the Rinaldi Lab at the University of Akron for running our powdered dye samples in their solid state NMR lab. Thank you to the Department of Chemistry & the Graduate School at YSU for the opportunity to return to my alma mater for further study in the sciences. I would like to acknowledge the Advanced Automotive Fuels Program in the U.S. Department of Energy for funding of our research. I am very appreciative of my thesis committee members, Drs. Sherri Lovelace-Cameron and Howard Mettee for their time and helpful suggestions and commentary.

I would finally like to thank all of my fellow members of the Linkous Group for their camaraderie throughout our many hours in the lab and office. To Dr. Linkous himself, I am eternally indebted. I thank him for all the opportunities he has given me throughout my time in the program. I have learned a great deal from him and not just about chemistry. I will continue to benefit from these experiences in the future.

To Paul

CHAPTER 1:
Introduction

The Hydrogen Economy:

Wood, charcoal, coal, gasoline, diesel, natural gas: all of these "carbon-based" fuel sources come from plants that covered the earth either recently (wood, charcoal) or eons ago (coal, gasoline, diesel, natural gas). For the latter, over geological time scales, dead plant matter was heated, compressed, and decomposed to create the coal beds, oil fields, and gas deposits that we tap today.

Converting all of this stored solar energy in the form of carbon fuels has created much geopolitical tension for two reasons; one a finite reality, and the other the threat of climate change. First, the coal, oil, and gas stores will run out someday; just when is hard to say, but it is safe to call these three fossil fuels finite, "non-renewable" forms of energy. The second issue with the Big 3 (coal, oil, gas) is global warming. Combustion of any of these fossil fuels results in carbon dioxide (CO_2) emissions, which are suspected to have played a leading role in the accelerating rise in average global temperatures since the early 20th century[1] which, many fear, will lead to long term climate change.

Though global energy consumption and greenhouse gas emissions have risen exponentially since the industrial revolution, CO_2 output per Watt generated has declined rather sharply, 0.3% annually since the mid 1800's.[2] This trend is called "decarbonization". The last, and most difficult, step is to use only hydrogen as a fuel:

$$2H_2 + O_2 \rightarrow 2H_2O$$

The benefits of complete decarbonization, the transition to the "hydrogen economy", are far reaching. The only byproduct of using hydrogen fuel is plain water. Less fuel[*] will be needed because of hydrogen's supreme energy content (see Table 1.1). A truly hydrogen economy generates no CO_2, drastically curbing greenhouse gas emissions; nor nitrogen oxides (NO_x's), or sulfur oxides (SO_x's), eliminating acid rain.

[*] By *weight*: H_2 is a very diffuse gas and larger *volumes* could be required

Oil spills will become a thing of the past; mountain top removal for coal and hydraulic fracturing for natural gas will become obsolete practices.

Table 1.1: Properties of common fuels[3,4,5]

Fuel	H:C Ratio	Energy Density (MJ/kg)	CO_2 Emission (g/MJ)
Wood (hardwoods)	0.1	10.5	108
Coal (anthracite)	0.5 – 1	30.2	112
Gasoline	2	44.4	85
Natural Gas	4	43	62
Hydrogen (H_2)	∞	120	0

As of 2006, production of hydrogen was 10.7 million metric tons annually.[6] One is tempted to ask; "why don't we simply ramp up production of hydrogen to meet our energy needs?" There are two problems with our hydrogen capacity today:
First, most of the hydrogen produced in today's economy, is dedicated to refining fossil fuels, treating metals, and in food production. The second problem lies in the true origins of our hydrogen today. The most cost effective way to produce hydrogen is through a process called steam reforming.[2] Herein, natural gas is heated with water vapor (steam) to yield hydrogen.

Steam reforming is not a sustainable way to produce hydrogen because it uses natural gas (methane), a fossil fuel. Despite plentiful gas reserves in the Marcellus and Utica shale deposits in the Eastern U.S. (among others around the world), which satiate sustainability concerns for the moment, steam reforming still generates CO_2, a greenhouse gas:

$$CH_4 + 2H_2O \rightarrow 4H_2 + CO_2$$

Another large scale means of producing hydrogen is via conventional water electrolysis, "water splitting". In a water splitting operation, two electrodes are submersed in an aqueous solution (water and electrolyte(s)) and powered by a DC

current. Despite being three times as expensive as steam reforming, conventional water splitting must, nearly always, be done with electricity from the grid.[2] Most of the electricity on the grid is produced via combustion of fossil fuels, which produce CO_2; using anything other than wholly renewable forms of energy leaves us in a carbon-logic loop. Sustainable production of *hydrogen* must occur outside of the *carbon* economy.

Solar Energy:

A great way to generate clean, renewable, carbon-free energy is via photovoltaic solar cell arrays. They could even be used to power an electrolyzer, representing a renewable source of hydrogen fuel. Several experimental attempts have been made to power electrolyzers with dedicated sources of renewable electricity.[7] As of yet, these projects have not proven to be economically feasible.

Though single and multicrystalline (Mc) silicon dominate over 80% of the current market for solar modules[8], the production impacts are much greater than of organic photovoltaic (OPV) technologies (polymer and dye-sensitized). The non-renewable energy use (NREU) required for production of the materials and assembly of the modules, along with corresponding CO_2 emissions, effectively represent the carbon footprint of the solar panels themselves. This is manifest in the "energy payback" period of the panel's operation. Energy from a solar panel, or any other renewable energy technology, really only becomes "clean" or "renewable" after it has paid back the energy that was required to manufacture and install the module. In Table 1.2, we can see that silicon based units require an energy payback period 7-10 times longer (vs. polymer) and 3-4 times longer (vs, dye-sensitized solar cells, "DSCs") than their organic counterparts. A comparative cost analysis is shown in Figure 1.3. These are the tremendous upsides that OPV technology possesses, despite poorer energy conversion efficiencies at the moment.

Table 1.2: Production impacts of select PV technologies[9]

	Polymer (flexible)	Mc-Si	CdTe (Thin Film)	CIS (Thin Film)	Si (Thin Film)	DSC (Thin Film)
NREU (MJ/W_p)	2.4	24.9	9.5	34.6	17.1	5.8
Spec. CO_2 Emissions ($g\ eq./W_p$)	132	1293	542	2231	993	255
Energy Payback Time (yrs.)	0.19	1.95	0.75	2.71	1.34	0.45

Table 1.3: Predicted future costs[†] of Mc-Si versus polymer PV[9]

PV type	2013-2020: Cost (€/W_p)	2030 and beyond: Cost (€/W_p)
Mc-Si	2.5-2.0	1.0-0.5
Polymer	0.5 – 1	<0.5

Though DSCs typically utilize thin films of metal oxide semiconductors, the materials used, and means of production are generally much cheaper than typical crystalline semiconductors and can be considered, along with polymer PV, as low-cost (and low carbon) PV technologies.

DSCs have steadily improved since Grätzel and O'Regan's seminal work in 1991. Their use of "mesoporous" titanium oxide electrodes improved efficiencies of DSC's by nearly an order of magnitude[10], unlocking a plethora of DSC research that continues today. Since then, research has focused on improving DSCs in every aspect of their operation and recently, solar power conversion efficiencies of over 12% have been recorded.[11]

[†] 2007€ per Watt Peak; excluding 'value added tax'

Water Splitting Solar Cells:

Photoelectrochemical water splitting (PECWS) was first reported 40 years ago by Honda and Fujishima by illuminating TiO_2 ("titania") with near-UV light.[12] Though sunlight does contain a small near-UV components (~5%), PECWS cells using only wide bandgap semiconductors such as TiO_2 (E_g ~ 3.0 eV) are drastically limited from the outset to maximum solar conversion efficiencies of ~2%.[13] To achieve effective water splitting on a large scale, PECWSs must be devised that can split water using light from a greater portion of the solar spectrum.

DSCs and PECWS cells are alike in that they are not truly "photovoltaic", but rather "photoelectrochemical" where charge is separated across a semiconductor/liquid junction. Solar irradiation excites electrons into the conduction band of the semiconductor, leaving holes behind in the valence band, from which the photoelectron originated. During forward operation of the cell, the photogenerated holes are replenished by oxidation of a redox active electrolyte; see Figure 1.1 below for a diagram of a typical DSC. The paradigm redox couple in DSCs has been the iodide/triiodide complex (I^-/I_3^-), though others have been developed.

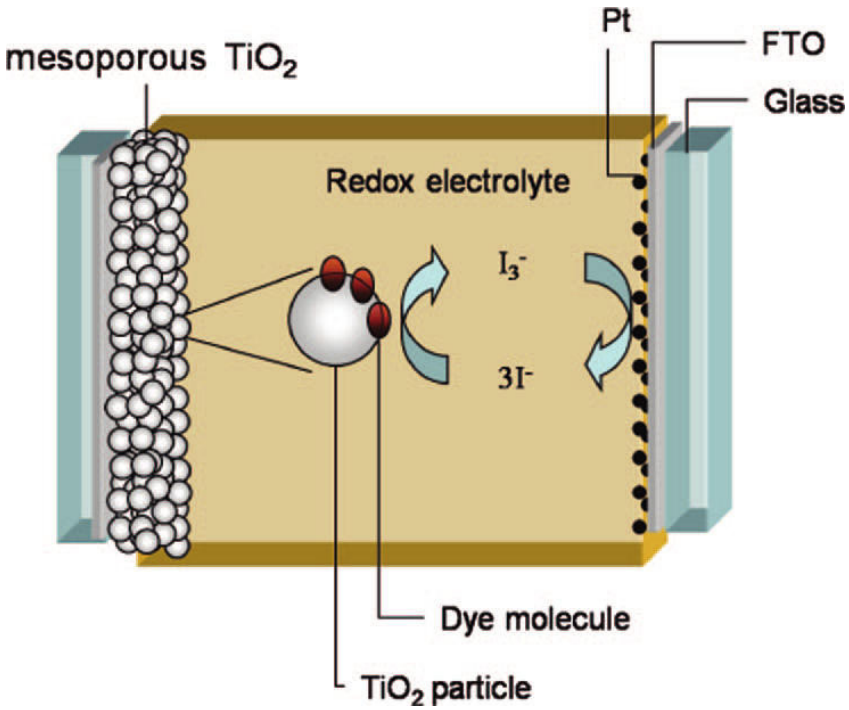

Figure 1.1: Diagram of a typical dye-sensitized solar cell[10]

The idea in PECWS is for the redox chemistry to be performed on water, splitting it into its constituent parts and providing hydrogen for use as stored solar energy:

$$2H_2O \rightarrow 4H^+_{(aq.)} + 4e^- + O_{2(g)} \qquad [E^0 = 1.23 \text{ eV}]$$
$$4H^+_{(aq.)} + 4e^- \rightarrow 2H_{2(g)} \qquad [E^0 = 0.00 \text{ eV}]$$

To drive the transfer of each electron in this process, a semiconductor must supply energy equivalent to at least 1.23 eV. Using the Planck relation, this would correspond to incident photons with wavelengths ≤ 1010 nm. To supply kinetic favorability to the reaction, and overcome inherent potential losses incurred during electron transfer, the energy required for watersplitting is reported to be 1.6 – 2.4 eV.[12] This corresponds to maximum photon wavelengths of 775-517 nm. Thus, in theory, much of the visible portion of the solar spectrum is energetically capable of water splitting.

Nano-structured titania has received much attention as a material for photoelectrochemical cells, particularly for DSCs, because of its high refractive index, chemical stability, low cost, and non-toxicity.[10] Concerning application in a PECWS

scheme, titania (TiO_2) alone is not capable of splitting water at appreciable efficiencies. With a large bandgap of 3.2 eV, the only light sufficiently energetic for charge separation comes from the UV portion of the solar spectrum where only about 5% of total solar energy lies. Here we run into a defining challenge of solar photocatalysis; the more useful and energetic the solar radiation (higher eV photons), the less there is to be had on earth's surface. Effective implementation of titania in a PECWS scheme will take advantage of the light in the visible spectrum inherently unavailable for photoelectrochemistry. This can be accomplished via "bandgap tuning" where the incorporation of guest dopants modify the electronic structure and electrochemical properties of the titania.

Another approach to enhancing the activity of titania is to adsorb chromophores onto the surface, like in a DSC [herein referred to as a dye-sensitized PECWS (DS-PECWS)]. These dye-sensitizers are charged with a few primary requirements:

First, they must be stable in aqueous solutions; also, their redox potentials must straddle those of water itself – the sensitizer should oxidize water, not be oxidized itself in the process. Second, the reduction potential of dye must be lower (more negative) than the conduction band (E_c) of the titania, that way charge transfer of photoexcited electrons from the dye into the titania is energetically favored. This is demonstrated in the energy band diagram in Figure 1.2. The dye should also be catalytic for the water splitting process. Mallouk *et al.*[13] have attached co-catalyst nanoparticles to a dye-sensitizer, itself attached to a titania electrode. Their dye of choice is a ruthenium tris(bipyridine) complex. Phosphonic acid groups solubilize the dye and chelate to the titania surface. To the opposite side of the dye is attached a malonate group, which served to chelate to the IrO_2 catalyst particle. A diagram of the cell is shown in Figure 1.2. Similar to Mallouk, the phosphonate group was chosen as the linkage for bonding to the titania surface. Phosphonate linkages provide enhanced sensitization efficiency and have been shown to possess an order of magnitude higher surface binding strength than typical carboxylate moieties.[14]

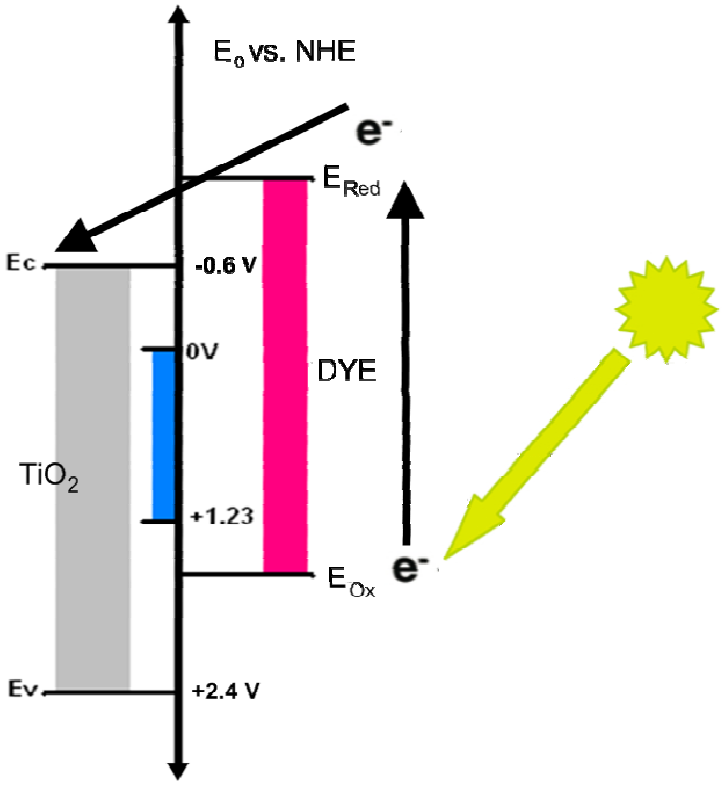

Figure 1.2: Energy diagram of a DS-PECWS Cell

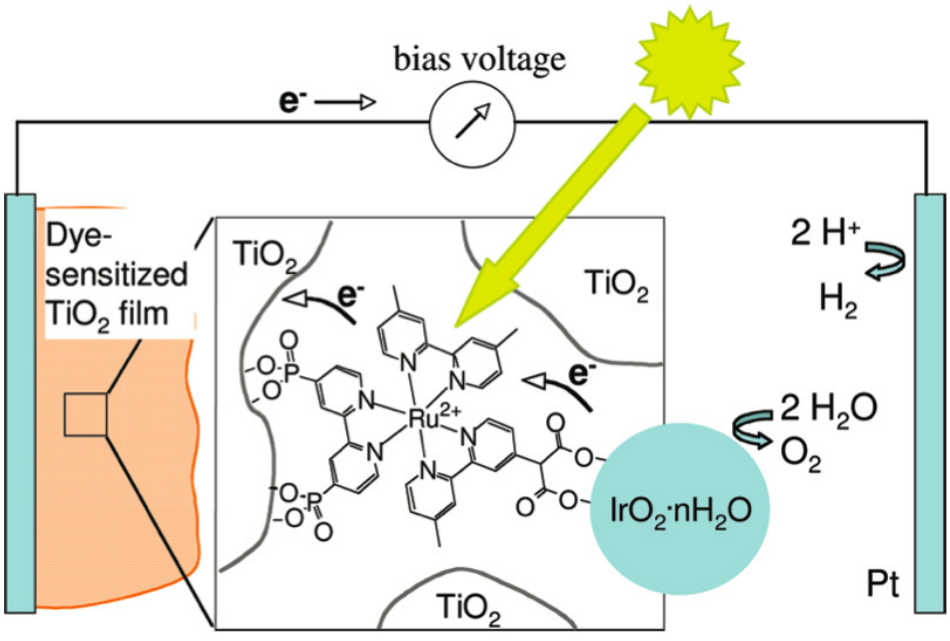

Figure 1.3: Diagram of a DS-PECWS cell[14]

The ultimate goal of our research is to investigate novel dyes for use in a similar DS-PECWS scheme. Perylene derivatives, on account of their excellent light absorption and charge transfer capabilities, have been widely studied for use in applications such as OLEDs, organic solar cells, dye lasers, and bio sensors.[15,16] A perylene diimide derivative, N,N'-Bis(3-phosphonopropyl)-3,4,9,10-perylenedicarboximide (pPDI), was synthesized and characterized to determine its viability as a water oxidation candidate. The *bis* structure of the pPDI molecule leaves the door open for future incorporation with a co-catalyst, similar to that described by Mallouk.

The objectives of this research are as follows:

1. To create high surface area TiO_2 electrodes for sensitization with the proposed dye.
2. To synthesize and characterize pPDI
3. To assess the viability of pPDI as a water oxidation candidate

CHAPTER 2
Experimental Procedures

2.1 Preparation and Characterization of Thin Film Titania (TiO_2) Electrodes

Thin films of titania were prepared on 1" square fluorine doped tin oxide glass [FTO] substrates using sols similar to those described in an existing procedure.[18] Two layers of titania are deposited onto the substrates. The first layer, thin, dense, and highly transparent, acts to block electrolyte contact with the conductive FTO thin film. The second is thick, mesoporous, and nearly opaque. The mesoporosity provides high surface area for dye adsorption while maintaining conductivity with the bulk.

Materials:

- Titanium tetraisopropoxide [TTiP] (99.999%, Aldrich)
- 50:50 n-butanol:ethanol (200 proof) mixture [BuOH/EtOH]
- Acetylacetone [AcAc] (≥99%, Aldrich)
- TiO_2 powder (P-25, Aeroxide)
- 1" × 1" × 3 mm FTO glass substrates (8 Ω/□, Hartford Glass)

Sol A Preparation:

First, 14.7 mL of BuOH/EtOH was added to 1.421 g (0.50 mmol) of TTiP. TTiP is stored under dry nitrogen to prevent hydrolysis. While stirring, 0.31 mL (0.30 mmol) of AcAc was added to the solution and stirred for an additional 30 min. AcAc acts to chelate the titania prior to sintering. 0.18 mL (1.0 mmol) of distilled, deionized water was added to the solution to hydrolyze the titanium.
The resulting molar ratio of the components, TTiP:AcAc:H_2O, is 1:0.6:2. The BuOH/EtOH renders a TTiP concentration of 0.3M.

Sol B Preparation:

Sol B was prepared like Sol A, but with (6.34 mL) BuOH/EtOH added such that [TTiP] = 0.6M.
208 mg of P-25 was slowly added to the solution under vigorous stirring. The resulting suspension must be heavily shaken prior to application.

Thin Film Preparation:

ITO substrates were cleaned by ultrasonication in deionized water, detergent, and acetone respectively.
A Chemat Technologies Model KW-4A spin coater was used in two stage mode for spreading the sols into thin films. Substrates are spun at 800 rpm for 10 s, then 2000 rpm for 20 s.
Substrates are placed in the spin coater, covered in a layer of Sol A using a Pasteur

pipette, and spun as described above. Next, the substrates were dried at 125 °C for 15 minutes. Then, using Sol B, three cycles of coating, spinning, and drying were performed.

After each spin coat, a round template is placed on the square substrates; sol left outside of the template is wiped off with acetone and cotton swabs, leaving a round layer of titania sol. This is done to allow the working brass contact to interface with the underlying FTO layer, rather than the titania itself. See Figure 2.1.1 below for a picture of the template.

Figure 2.1.1: Photo of electrode template

The electrodes were then placed in a tube furnace (Lindberg Model 54233, with Eurotherm Model 2404 programmable controller) to remove remaining organics and sinter the titania particles. A ramp up (10 °C/min), dwell (500 °C, 1 hr.), ramp down (10 °C/min) sequence was programmed into the controller for the sintering procedure. Following sintering, the substrates were washed with deionized water and acetone, and then dried.

Mass of Titania Layers:

Several substrates were weighed before and after spin coating to determine the mass of the titania layers. The mass of the dense titania layers (from “Sol A”) is negligible.

Table 2.1.1: Masses of select substrates

Substrate	Mass, Plain FTO (g)	Mass, FTO + TiO_2 (g)	Mass of TiO_2 (g)
Ti4.2	5.1051	5.1069	0.0018
Ti4.3	5.1584	5.1601	0.0017
Ti4.4	5.1791	5.1809	0.0018
Ti4.6	5.1230	5.1249	0.0019
Ti4.7	5.1390	5.1409	0.0019

The average mass of the porous titania layers is 1.8 mg. All layers are 22 mm in diameter. The density of titania layers is thus 2.62 g/cm^3; the theoretical density of solid TiO_2 is 4.23 g/cm^3.

Profile scans of substrates were taken with a TLA Tencor D-100 profilometer, in Step-Up mode. Figures 2.1.2 and 2.1.3 below show a profile of a plain FTO substrate at two different vertical scales. Next, in Figures 2.1.4 and 2.1.5, are profiles of a plain, thin titania electrode. Again, a baseline is seen that is flat within 100 nm except a spike in the graph at 1.8 mm into the scan. This represents the crumpled edge of the electrode, caused by contact of the thin, beveled edge of the template shown in Figure 2.1.1. The height of the edge, measured from the FTO surface, is 246 nm; see Figure 2.1.6 below. Aside from this edge, the substrate is also shown to be flat with about 100 nm. A small step from before the edge (< 1.6 mm) to after the edge (>1.9 mm) is observed. This was measured to be 18 nm with 1.5 mm wide cursors on either side of the higher edge; see Figure 2.1.7 below. The average thickness of a thick, mesoporous titania electrode is measured to be 1.8 µm. See figure 2.1.8 below for a representative profile of a porous titania layer (sample Ti4.6).

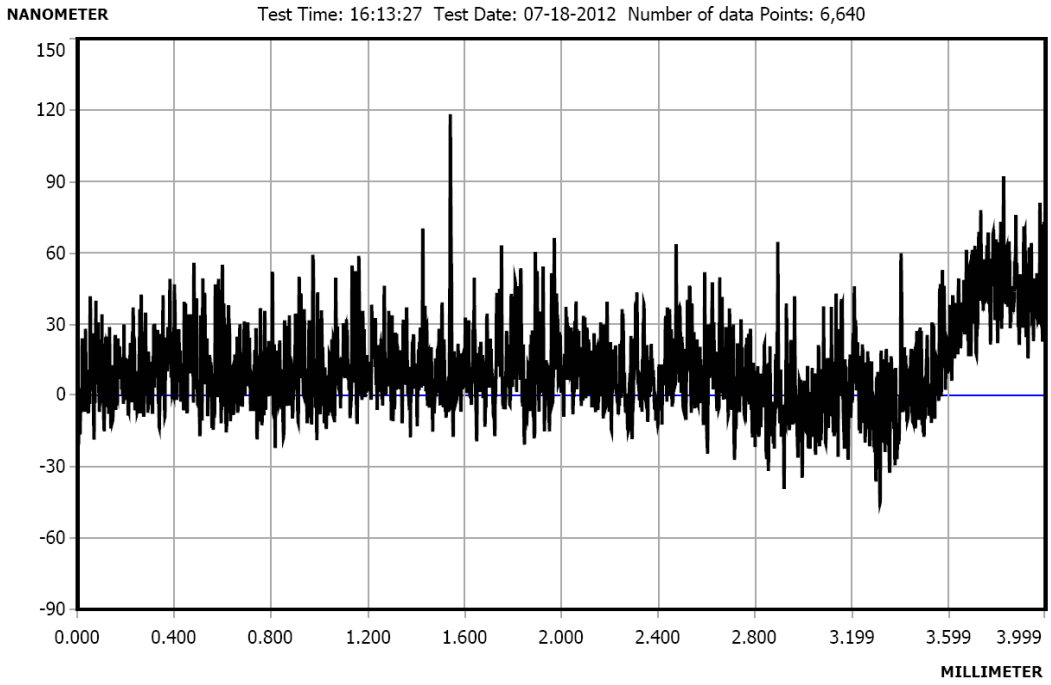

Figure 2.1.2: Profile of a plain FTO substrate, small scale

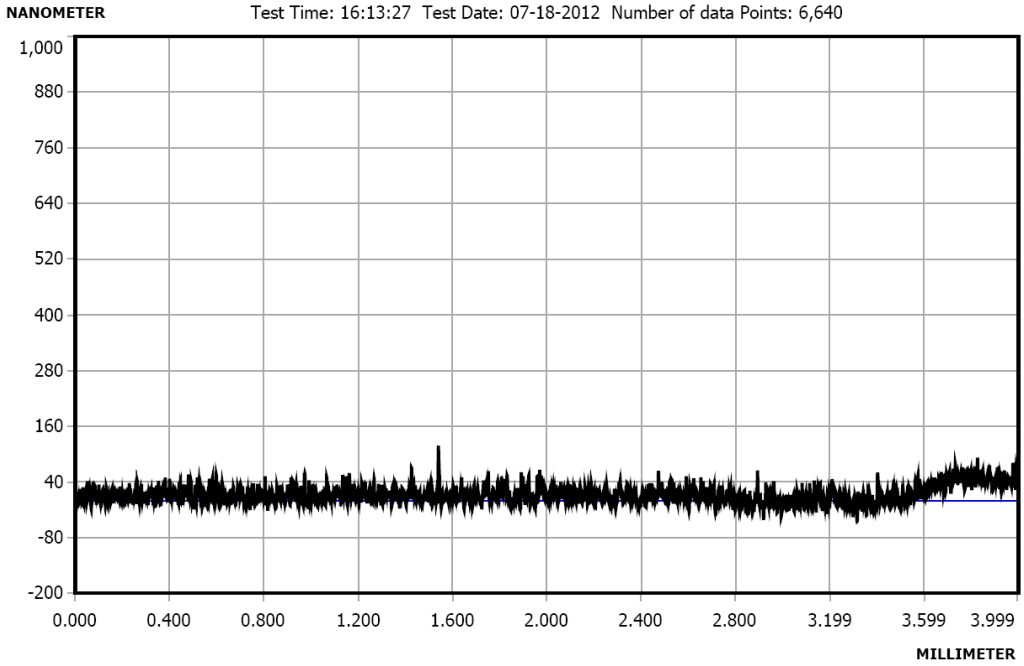

Figure 2.1.3: Profile of a plain FTO substrate, medium scale

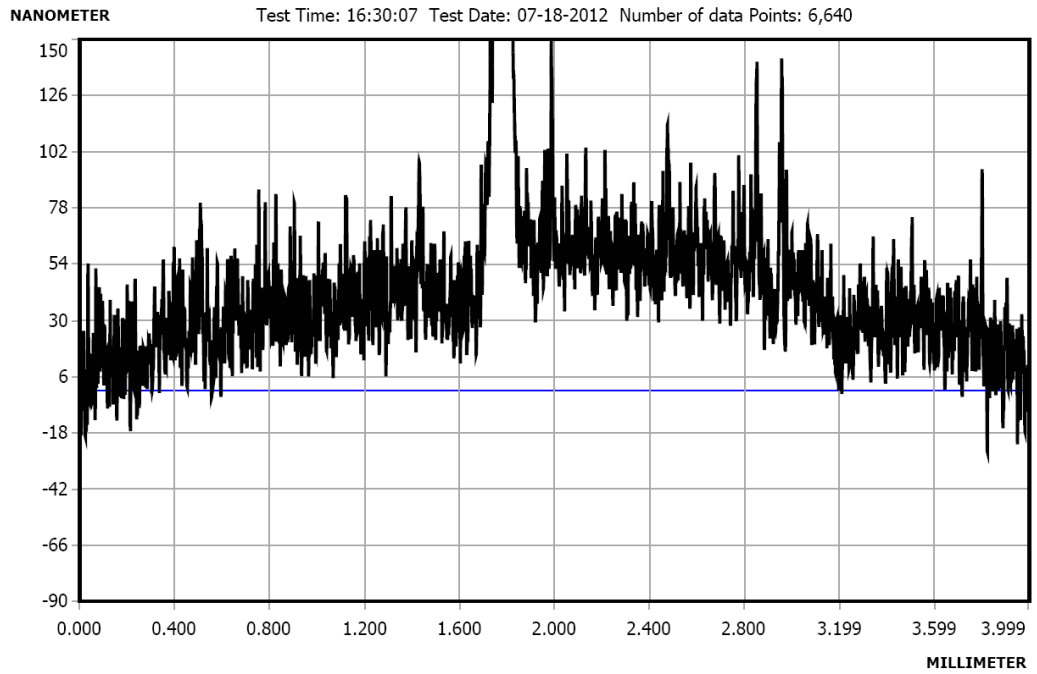

Figure 2.1.4: Profile of Ti5.0, small scale

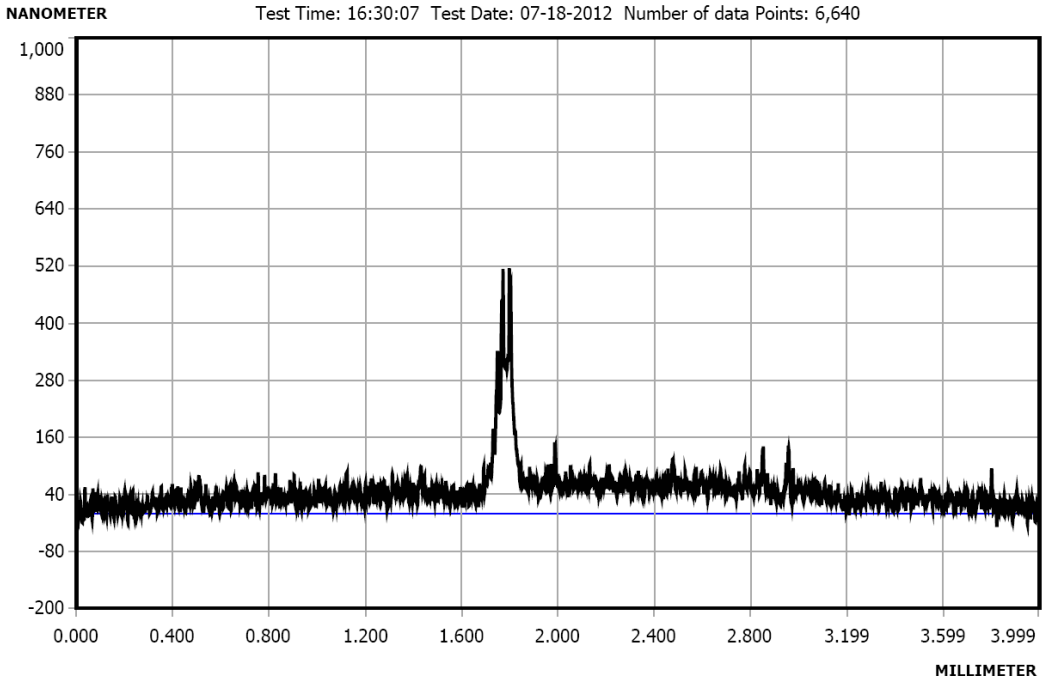

Figure 2.1.5: Profile of Ti5.0, medium scale

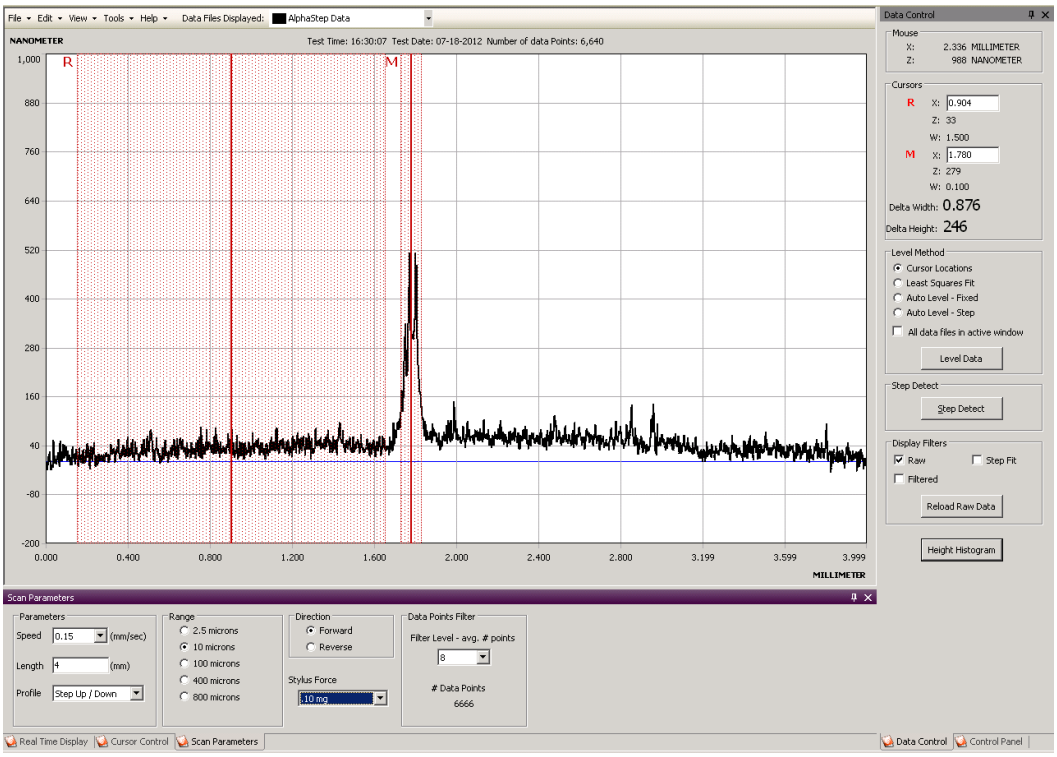

Figure 2.1.6: Interfacial step-up measurement of Ti5.0 (screen shot)

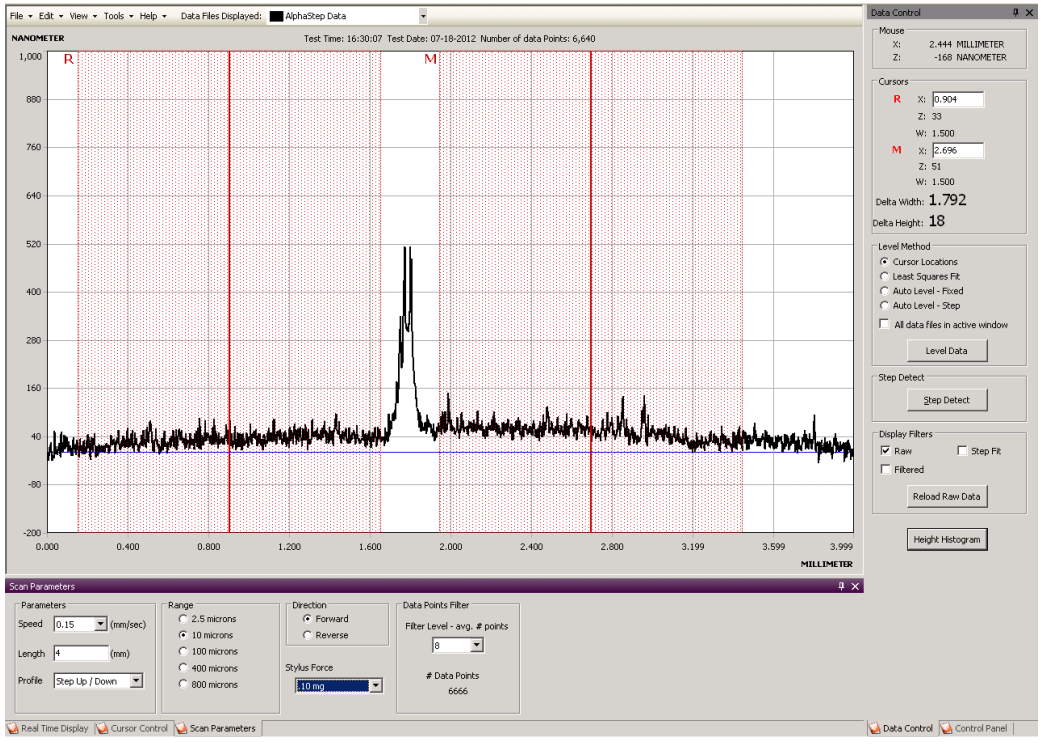

Figure 2.1.7: Bulk step-up measurement of Ti5.0 (screen shot)

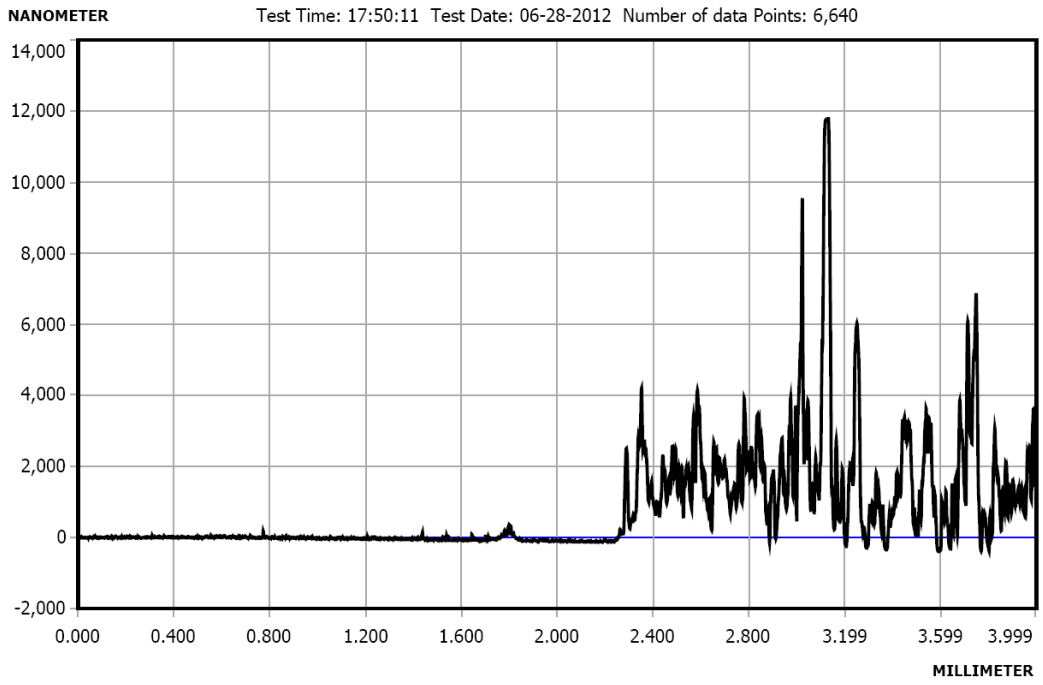

Figure 2.1.8: Profile of Ti4.6

The substrates at their various stages of development were examined with a scanning electron microscope, SEM (JEOL, JIB 4500 MultiBeam). Elemental analysis of micrographs was obtained with an energy-dispersive X-ray spectrometer, EDX (EDAX, Si-drift detector). The first SEM shown (Figure 2.1.9) is a plain FTO substrate revealing FTO particles of 100 nm size. The elemental composition is shown below the image (Table 2.1.2).

The second image, of a single dense layer of TiO_2 (Figure 2.1.10), shows a uniform layer of TiO_2 particles of 100 nm diameter. The corresponding EDX data is listed in Table 2.1.3

The third image, at much lower magnification, shows the surface of a porous TiO_2 electrode (Figure 2.1.11). The fourth image, at similar magnification, shows the nanostructure of one of the “islands” amongst the porous layer (Figure 2.1.12). The EDX results in Table 2.1.4 are almost exclusively from titania, though with traces of the underlying glass and FTO layer (Si and Sn signals). Particle size is larger (~200 nm) for the porous layer, though within an order of magnitude.

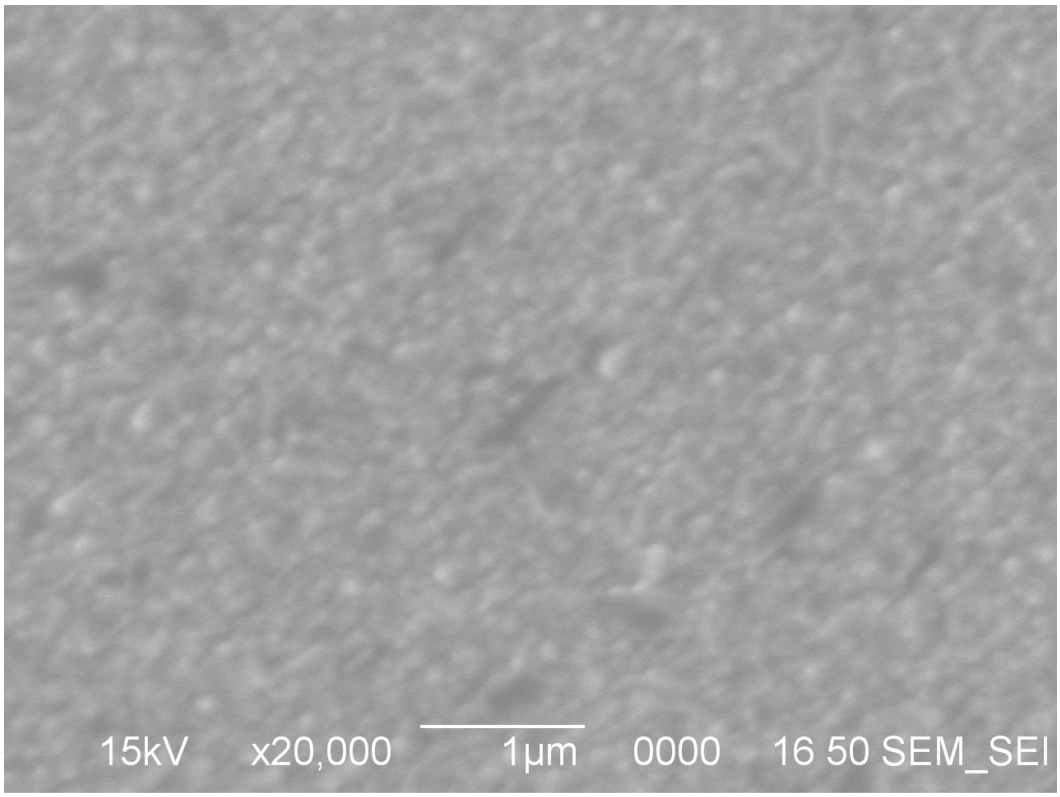

Figure 2.1.9: SEM of an FTO substrate (20,000x)

Table 2.1.2: EDX analysis an FTO substrate

Element	Weight %	Atomic %
C (K)	2.43	6.29
N (K)	8.73	19.39
O (K)	27.36	53.20
Si (K)	5.92	6.55
Sn (K)	55.56	14.56

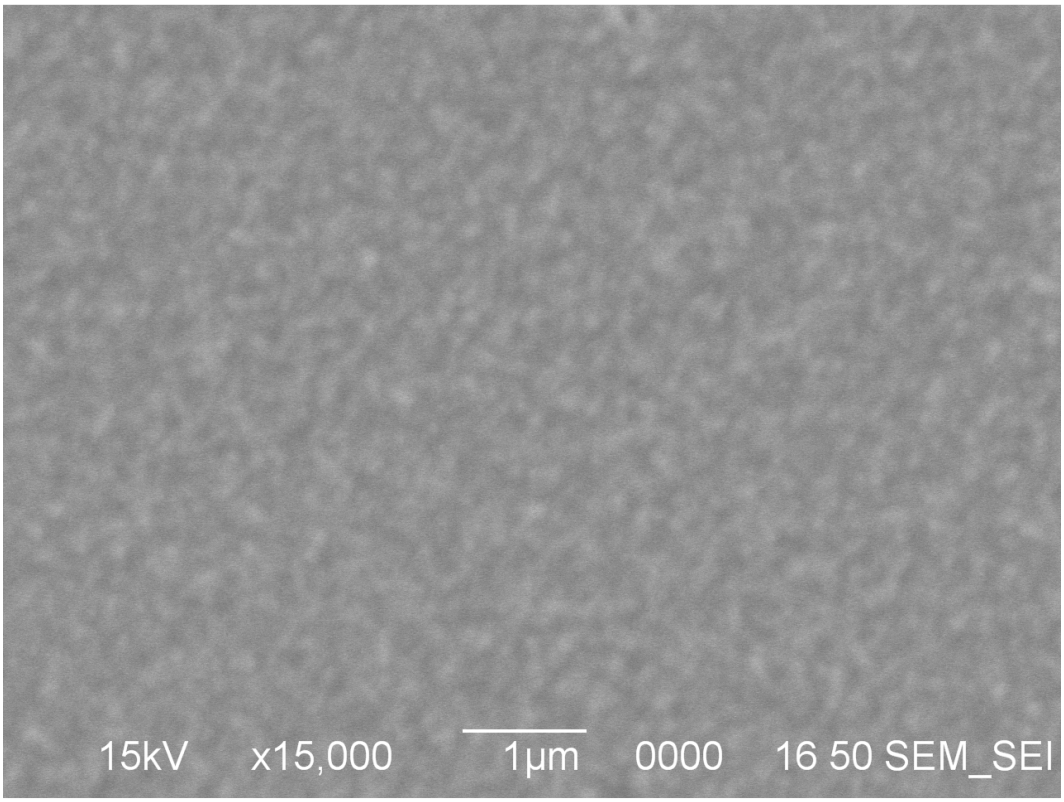

Figure 2.1.10: SEM of a dense titania film (15,000x)

Table 2.1.3: EDX analysis of a dense titania film

Element	Weight %	Atomic %
C (K)	2.94	8.86
N (K)	0.00	0.00
O (K)	27.76	62.85
Si (K)	5.42	6.99
Sn (K)	59.90	18.28
Ti (K)	3.99	3.01

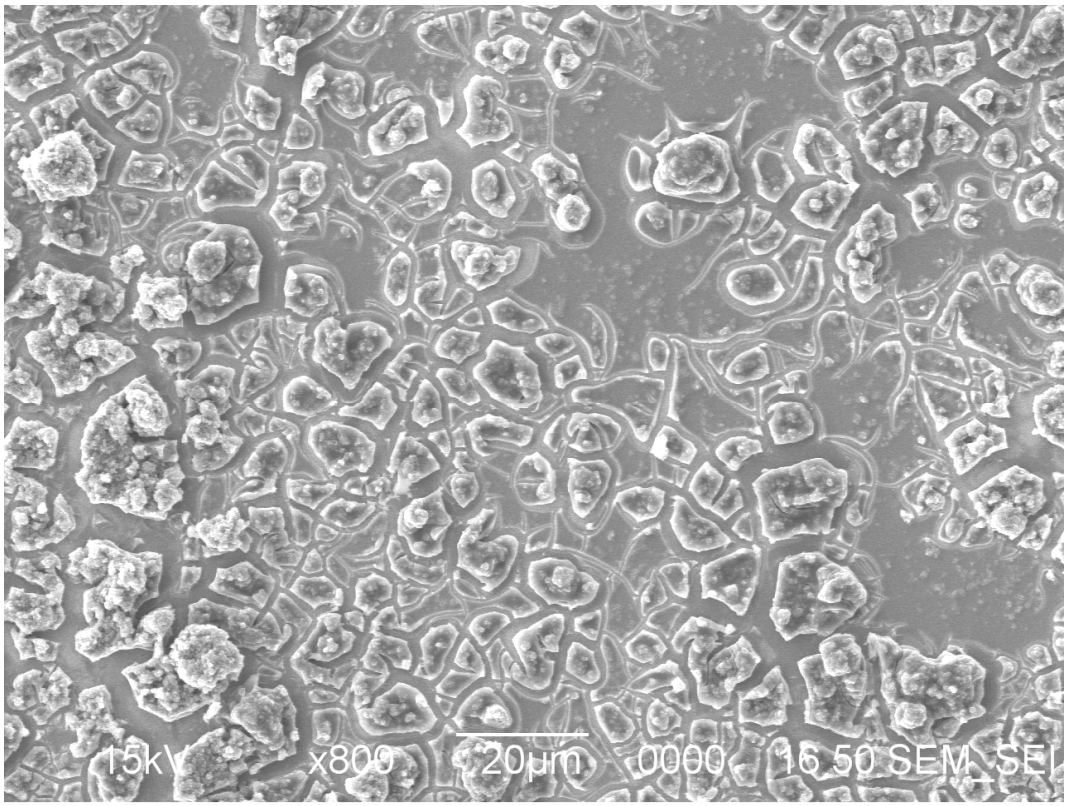

Figure 2.1.11: SEM of a porous titania film (800x)

Table 2.1.4: EDX analysis of a porous titania film

Element	Weight %	Atomic %
O (K)	54.70	78.52
Si (K)	0.58	0.48
Sn (L)	1.52	0.29
Ti (K)	43.20	20.71

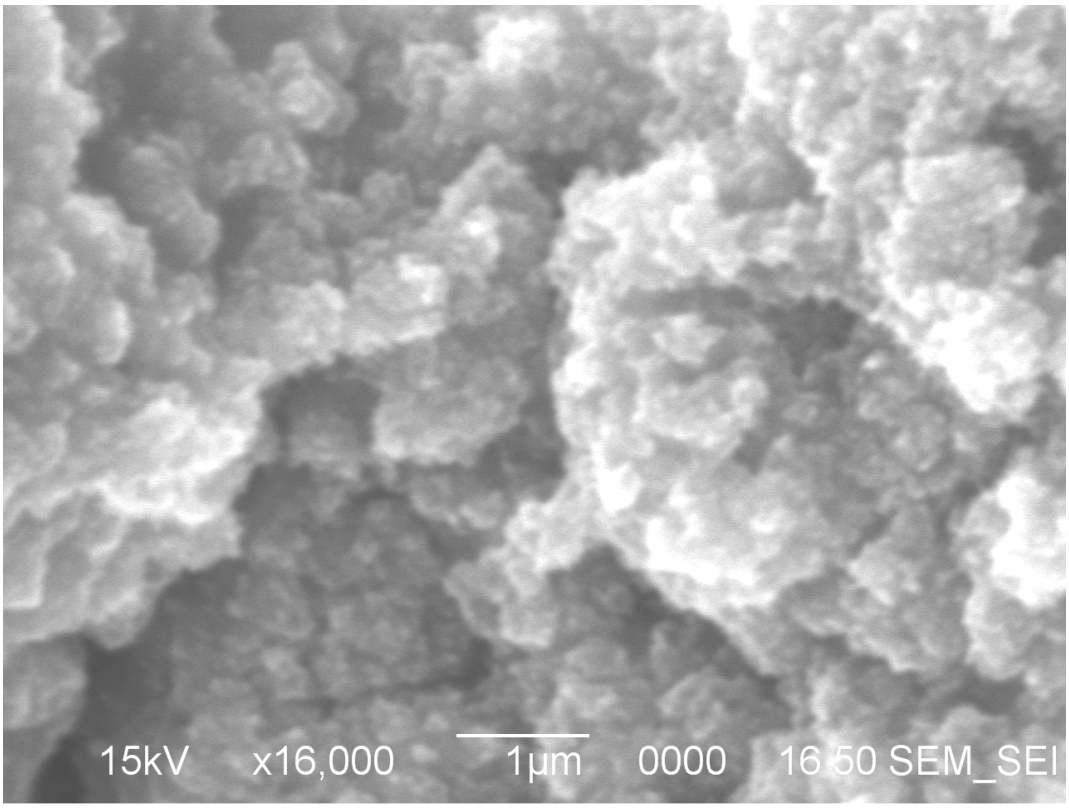

Figure 2.1.12: SEM of a porous titania film (16,000x)

Creation of high surface area electrodes for dye sensitization is desirable because it enables more adsorbed dye to be exposed to the cell environment. This allows for greater light absorption and should yield improved photoelectrochemical activity. The SEM images described above demonstrate the much improved electrode surface of the porous titania electrodes compared with the dense, flat electrode.

Quantification of this surface area increase is done through capacitance measurements. The surface area of an electrode is directly proportional to the electrode capacitance. The current at zero potential reveals the electrode capacitance as a function of the voltage sweep scan rate, v. At E = 0 V:

$$i = vC$$

Cyclic voltammograms of a porous titania electrode (1 coat Sol A, 3 coats Sol B) are taken at different scan rates (100, 50, and 25 mV/s). The magnitude of current when both the forward and reverse sweeps cross the y-axis (E = 0 V) is measured and used to determine the capacitance of the electrode. A summary of the results is shown below in Table 2.1.5. Similarly, a dense titania electrode (1 coat Sol A) was measured at the three scan rates; these results are shown in Table 2.1.6. Close-ups of the CVs used for these measurements are shown below in Figures 2.1.13 and 2.1.14. Scan rates of 25 mV/s are shown in blue, 50 mV/s in red, and 100 mV/s in black. Capacitance is shown with

respect to the electrode area. The electrodes are 22 mm in diameter (3.8 cm^2).

Table 2.1.5: Capacitance measurements, Ti4.1 (porous titania)

Sweep Rate (mV/s)	I (μA)	C(μF)	C/A (μF/cm^2)
25	55	2,200	580
50	50	1,000	260
100	54	540	140

Table 2.1.6: Capacitance measurements, Ti5.0 (dense titania)

Sweep Rate (mV/s)	I (μA)	C(μF)	C/A (μF/cm^2)
25	32	1,300	330
50	31	620	160
100	34	340	88

The difference in capacitance from the flat, two dimensional dense titania layer, to the thicker, porous electrode indicates the increase in surface area provided by the nanostructured particles. These results are summarized in Table 2.1.7 and indicate a 60-70% increase in electroactive surface area.

Table 2.1.7: Capacitance comparison of titania electrodes

Sweep Rate (mV/s)	Ti4.1 : Ti5.0 C/A (μF/cm^2)
25	1.7
50	1.6
100	1.6

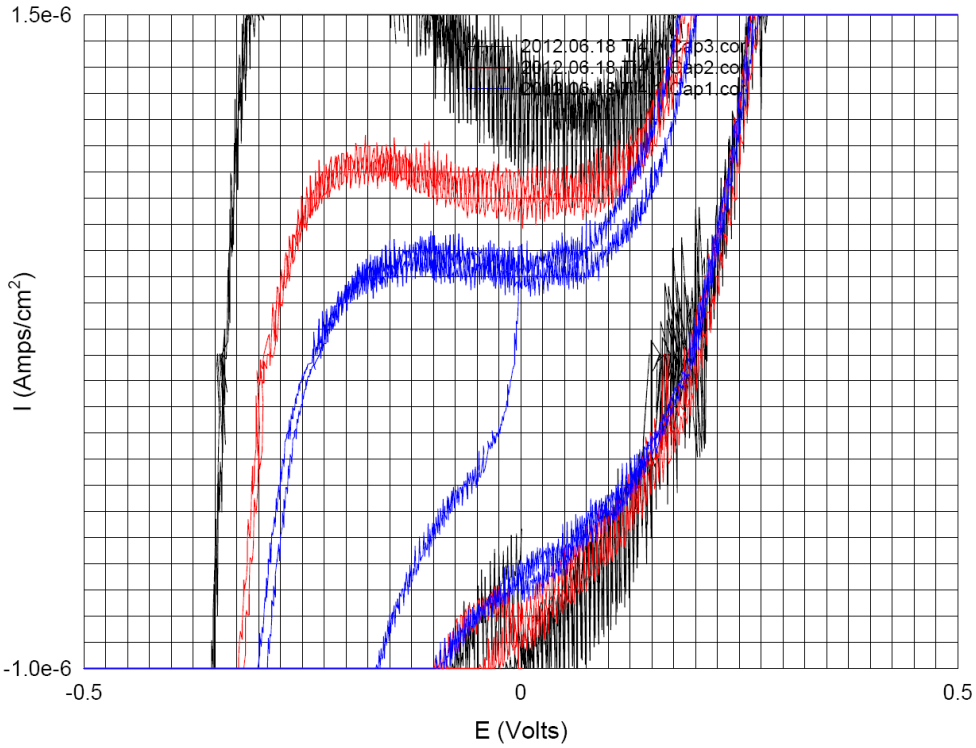

Figure 2.1.13: CVs of Ti4.1 at different scan rates

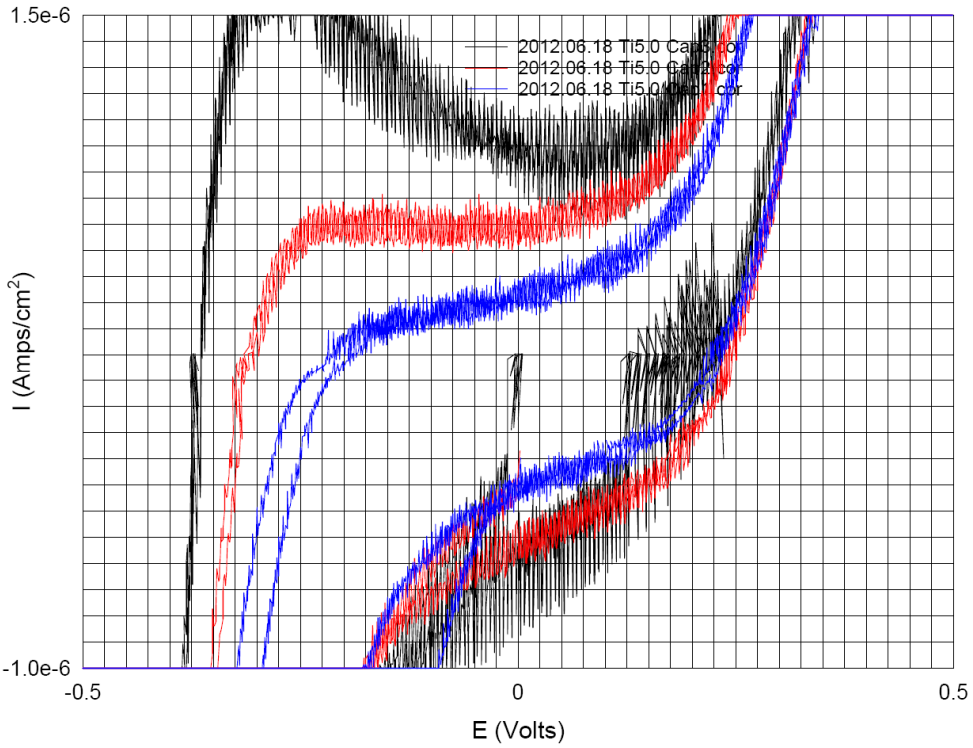

Figure 2.1.14: CVs of Ti5.0 at different scan rates

2.2 Synthesis and Characterization of N,N'-Bis(3-phosphonopropyl)-3,4,9,10-perylenedicarboximide (pPDI)

Background:

A previous synthesis of pPDI has been described for use in a bulk heterojunction of an organic photovoltaic (OPV) system.[19] We have replicated the synthesis to examine the viability of pPDI as a water oxidation candidate for use in the visible light water splitting scheme previously described.

Experimental Procedure:

In a 250 mL round bottom flask was placed:

- 0.962 g Perylene-3,4,9,10-tetracarboxylic dianhydride (PTCDA)
- [97% Aldrich, 2.405 mmol]
- 0.980 g 3-aminopropylphosphonic acid (3-APPA)
- [98% Aldrich, 7.04 mmol, 2.9 equivalents]
- 10 g imidazole

The mixture was heated to 100 °C and stirred for 4 h.

After cooling to room temperature, the mixture was removed from the reaction flask by dissolving with 75 mL water and ultrasonication. Next, 75 mL THF was added to the aqueous solution to precipitate the product which was then filtered. The product was washed with THF and EtOH to remove imidazole and any remaining 3-APPA.

Further purification of the product via liquid chromatography (LC) was complicated due to very low solubility (<100 μM).

See Figures 2.2.1 and 2.2.2 below for drawings of the structures of PTCDA and pPDI.

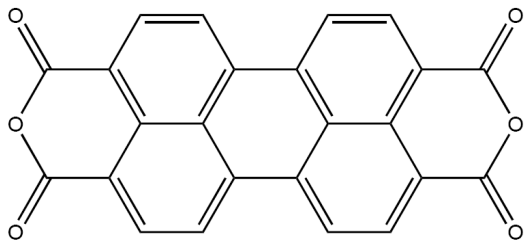

Figure 2.2.1: Structure of Perylene-3,4,9,10-tetracarboxylic dianhydride (PTCDA)

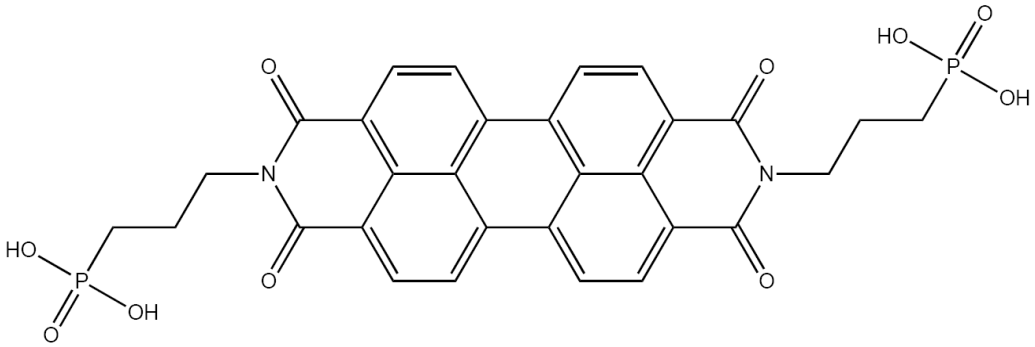

Figure 2.2.2: *N,N'*-Bis(3-phosphonopropyl)-3,4,9,10-perylenedicarboximide (pPDI)

Mass Spectrometry:

An aqueous solution of pPDI was analyzed by direct injection into a Bruker Esquire-LC ion trap mass spectrometer equipped with an Agilent 1100 liquid chromatograph (LC). The solvent flow rate through the LC was 10 µL/min (methanol). The pPDI sample flow rate was 250 µL/h; nebulizer pressure was 20.0 psi. Spectra were taken in negative mode with a dry He at 7.00 psi and 325 °C.

Displayed in Figure 2.2.3 below is a mass spectrum of pPDI. The large peak at 633 mass to charge ratio (m/z) corresponds to $[pPDI]^{1-}$. The 511 m/z corresponds to the anion of an *N*'-mono(3-phosphonopropyl)-3,4,9,10-perylenedicarboximide. Likewise, the 389 m/z corresponds to the anion of simply perylenedicarboximide. The 633 m/z was isolated for fragmentation, shown in Figures 2.2.4 and 2.2.5.

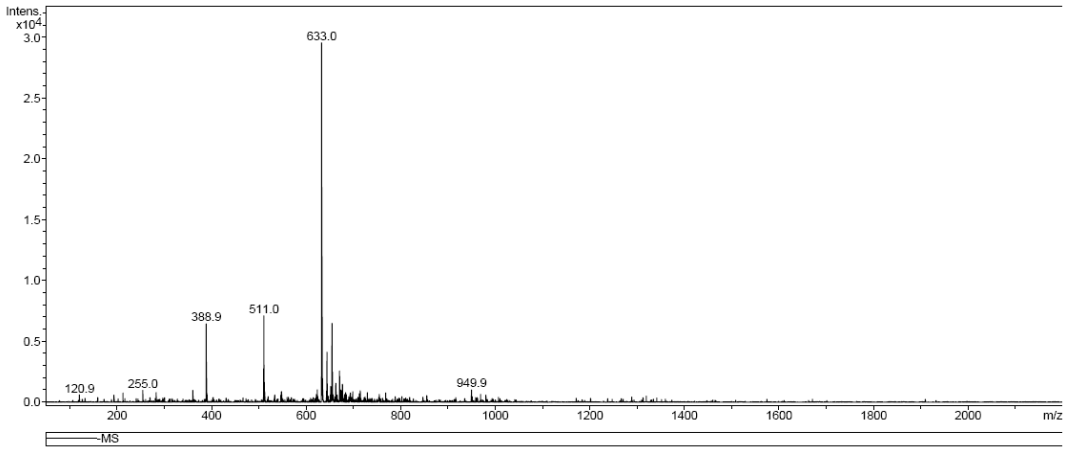

Figure 2.2.3: Mass Spectrum of pPDI

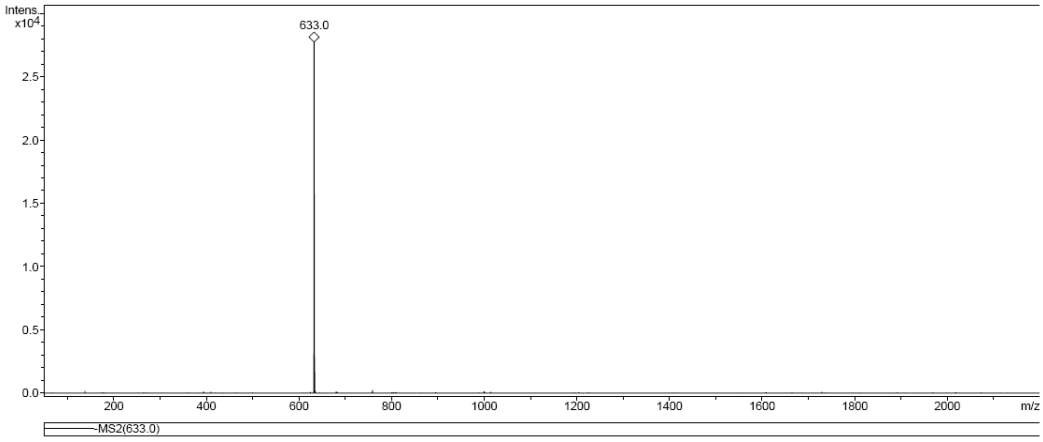

Figure 2.2.4: Isolation of 633 m/z

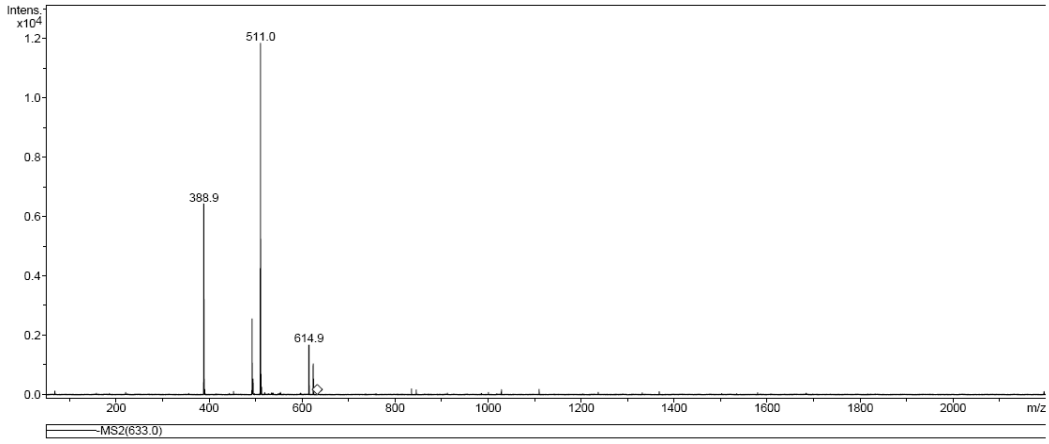

Figure 2.2.5: Fragmentation of 633 m/z

Gel Electrophoresis:

Aqueous suspensions of 3 mM pPDI were prepared at neutral and at pH 9. Different aliquots of the two solutions were placed into a gel electrophoresis apparatus to form five lanes. These are described in Table 2.2.1 below. A photograph of the agarose template after completion of the experiment is shown in Figure 2.2.6.

Table 2.2.1: Gel electrophoresis samples

Lane (left to right)	1	2	3	4	5
pH	7	7	9	9	9
Sample Volume (μL)	20	10	10	20	30

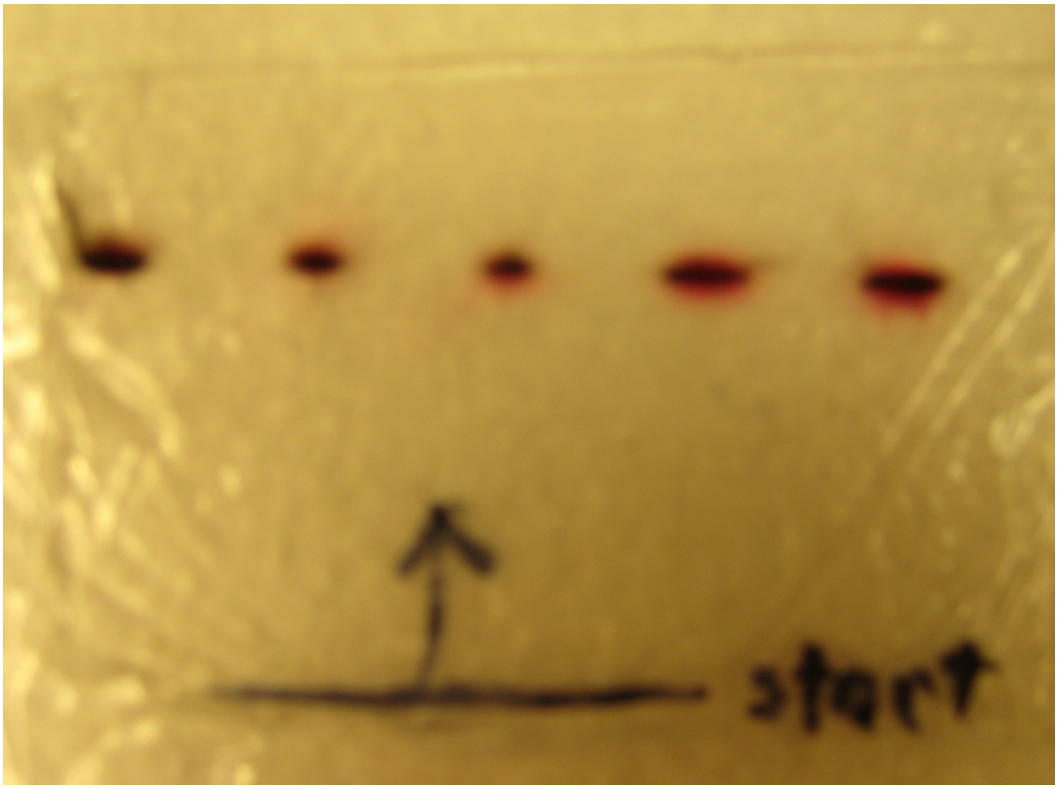

Figure 2.2.6: Samples of pPDI after gel electrophoresis

Nuclear Magnetic Resonance (NMR):

The starting material PTCDA is insoluble, making liquid ^{1}H characterization impossible. However, characterization of the reagent 3-APPA is facile due to its excellent solubility. NMR spectra were taken of 3-APPA and compared with the presumed reaction product, pPDI.

Nuclear magnetic resonance spectra of liquid samples were taken using D_2O as a solvent on a Bruker Avance III system. The ^{1}H spectrum was taken at 400 MHz; the ^{31}P spectra at 162 MHz. All chemical shifts (δ) are reported in parts per million (ppm). Signals are labeled as follows: s (singlet); t (triplet); q (quintet); m (multiplet); bm (broad multiplet).

^{1}H NMR of 3-APPA (Figure 2.2.7):

δ 1.64 (q, 2H, C-CH_2-$PO(OH)_2$), 1.89 (m, 2H, C-CH_2-C), 3.06 (t, 2H, CH_2-N).

^{1}H NMR of pPDI (Figure 2.2.7):

δ 1.9 (bm, 8H, C-CH_2, C-CH_2-$PO(OH)_2$), 3.9 (bm, 4H, $(RC=O)_2N$-CH_2), 7.5 (bm, 8H, Ar-H), 8.7 (s, 4H, P-OH).

^{31}P NMR of 3-APPA (Figure 2.2.8):

δ 23.7 (s, R-$PO(OH)_2$)

^{31}P NMR of pPDI (Figure 2.2.9):

δ 24.8 (s, R-$PO(OH)_2$)

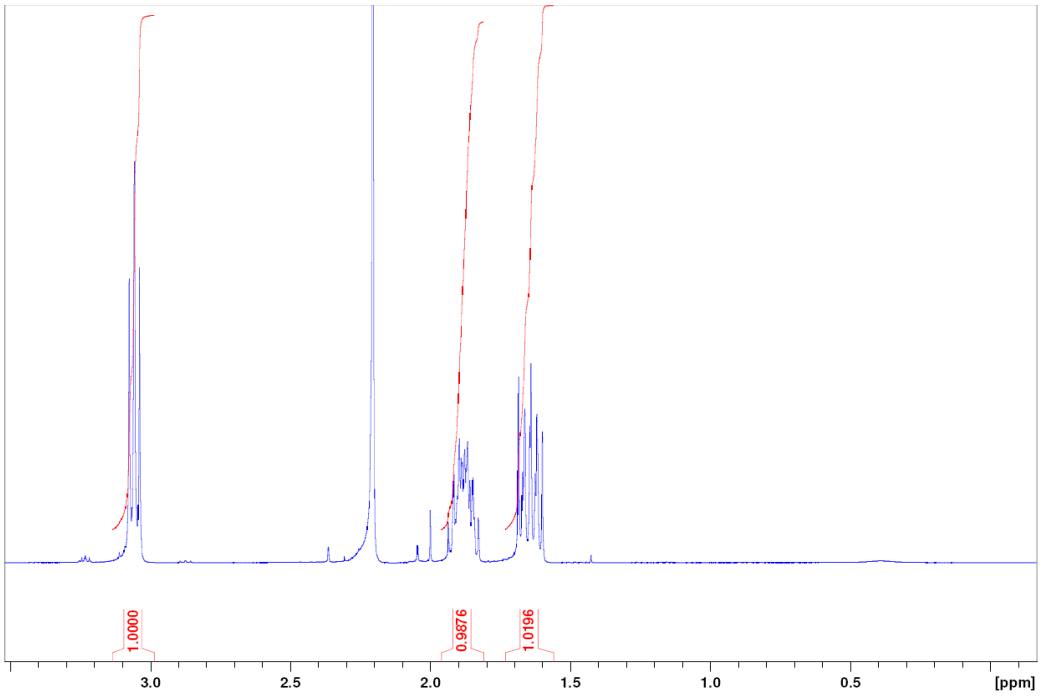

Figure 2.2.7: ^{1}H NMR spectrum of 3-APPA

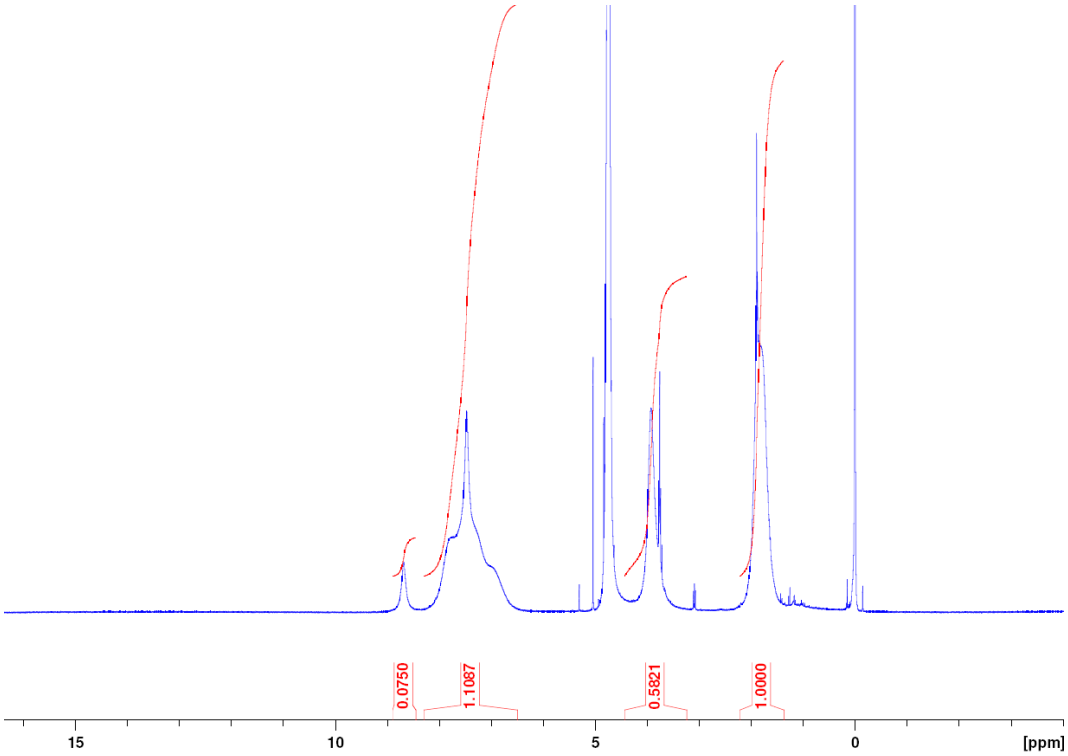

Figure 2.2.8: ^{1}H NMR spectrum of pPDI

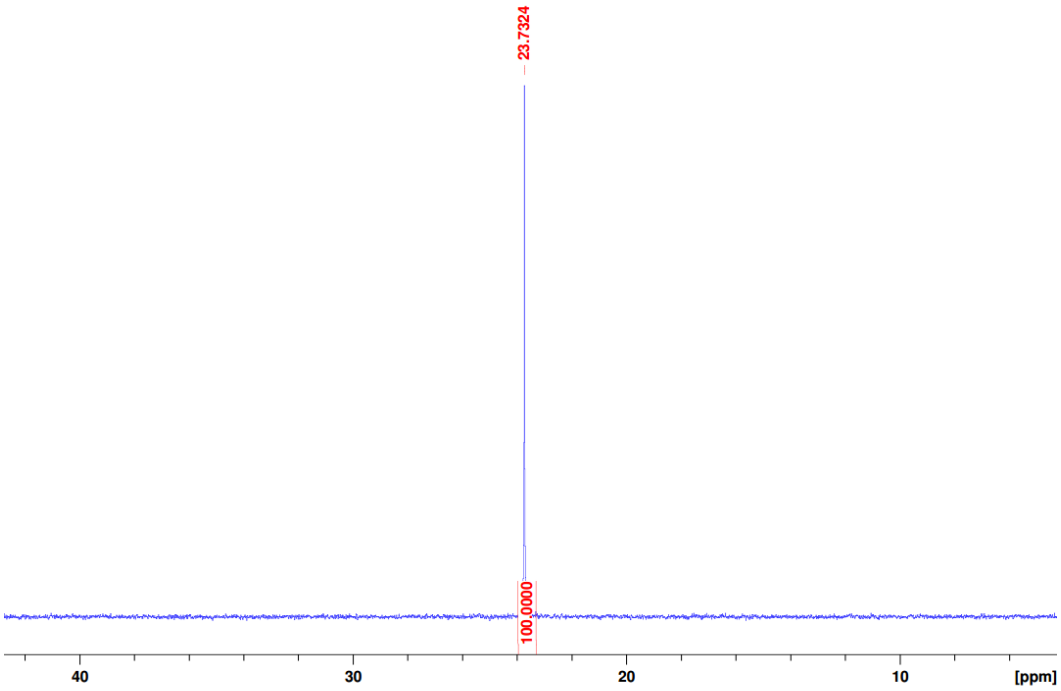

Figure 2.2.9: ^{31}P NMR spectrum of 3-APPA

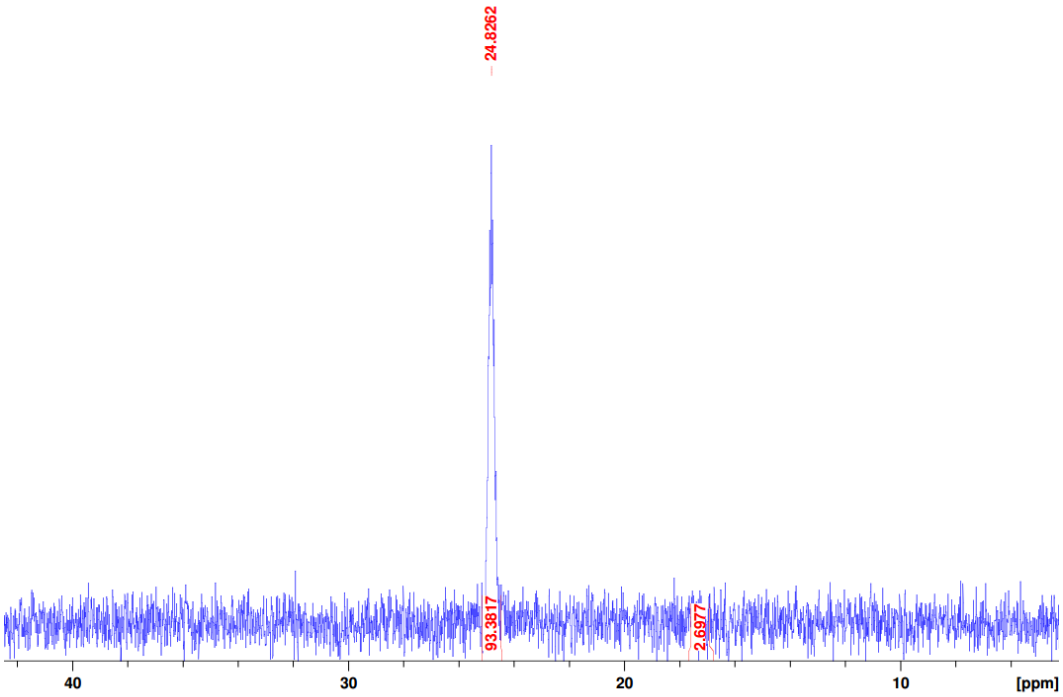

Figure 2.2.10: ^{31}P NMR spectrum of pPDI

Solid State NMR:

Solid NMR spectra of powders of both PTCDA and pPDI were performed on a Varian NMRS 500-02 spectrometer. ^{13}C spectra were taken at 125.69 MHz; 50 kHz sweep width; 10 kHz spin rate; 0.01536 s acquisition time; 4 s recycle delay; 2724 scans, pPDI; 2436 scans, PTCDA.

Symmetry is expected for both PTCDA and pPDI along both the long and short axes of the molecules. This is demonstrated in Figure 2.2.10 below. PTCDA has 7 unique carbons, 2 with single symmetry (shown in red) and 5 with double symmetry (shown in blue). Similarly, for pPDI, 10 unique carbon signals are expected with 3 additional carbons from the alkylphosphonic acid chain. Spectra for PTCDA and pPDI are shown in Figures 2.2.11 and 2.2.12.

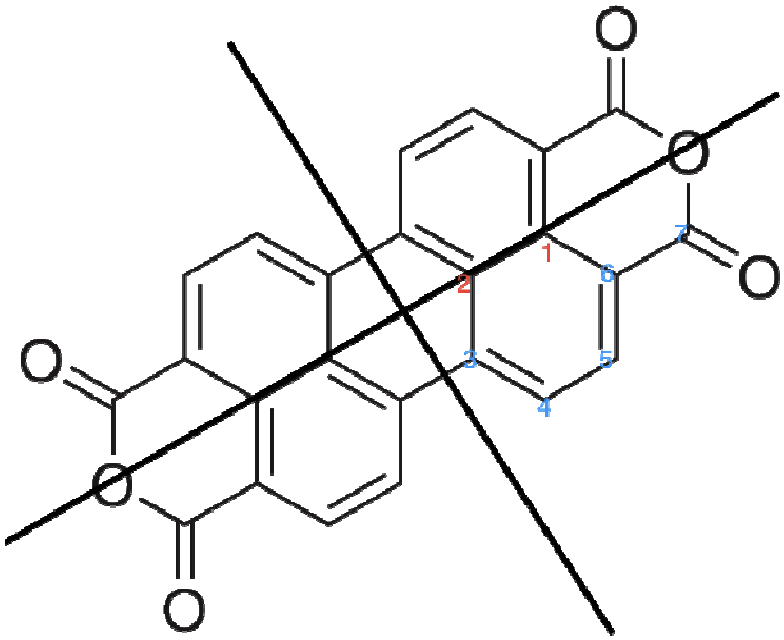

Figure 2.2.11: ^{13}C symmetry of PTCDA

^{13}C NMR of PTCDA:

δ 117, 124, 127, 128, 135, 135, 160

^{13}C NMR of pPDI:

δ 25, 28, 41, 79, 89, 117, 122, 126, 127, 129, 132, 136, 162, 167, 169, 173, 178, 207, 213, 222

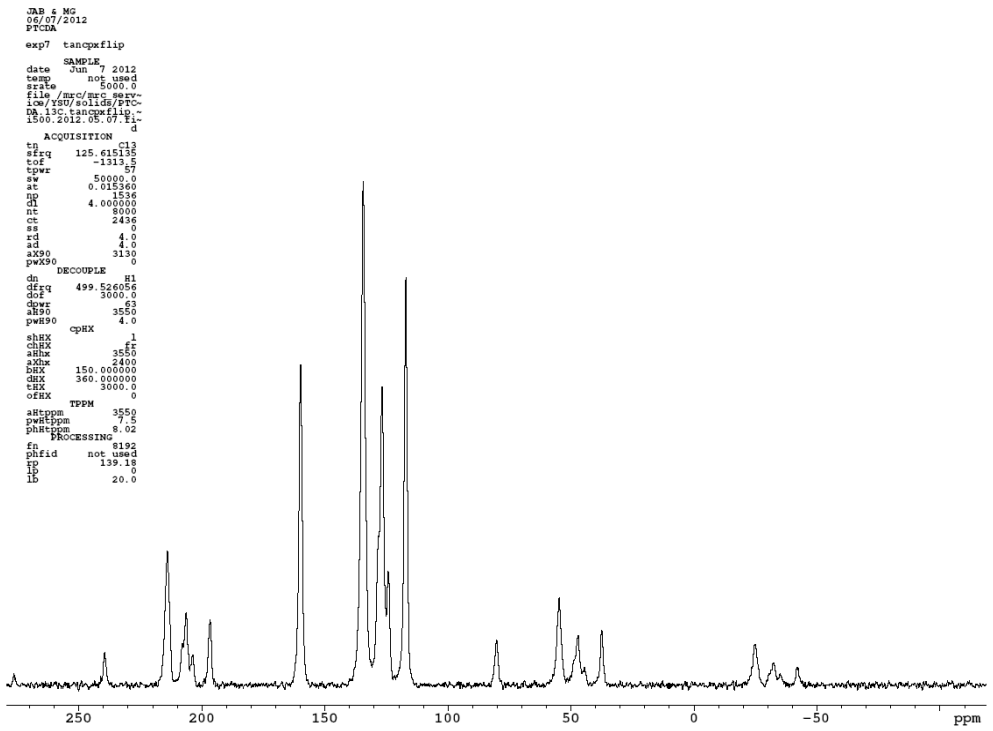

Figure 2.2.12: Solid ^{13}C spectrum of PTCDA

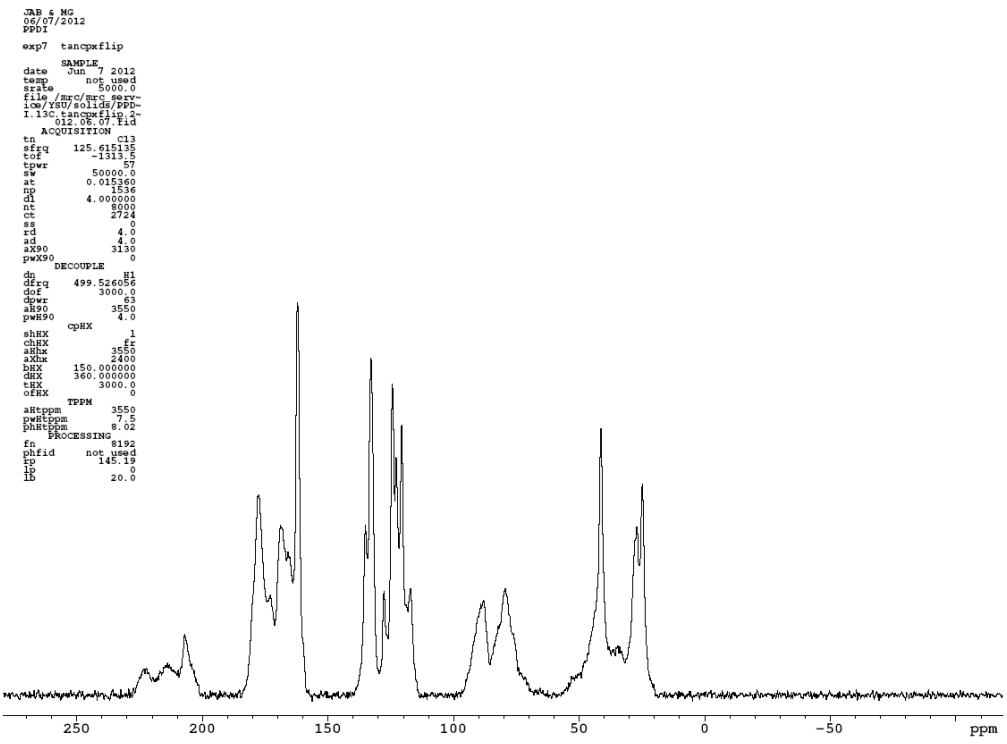

Figure 2.2.13: Solid ^{13}C spectrum of pPDI

Infrared Spectroscopy (IR):

Nujol mineral oil mulls of both PTCDA and pPDI were made; one drop of each mull was placed between NaCl plates for the respective spectra. Figure 2.2.13 below shows overlaid spectra of PTCDA (red) and pPDI (light blue). A single drop of Nujol between the salt plates was used as a background. A spectrum was taken of the Nujol oil against the Nujol background. This spectrum is shown in dark blue below and represents the baseline of the experiment.

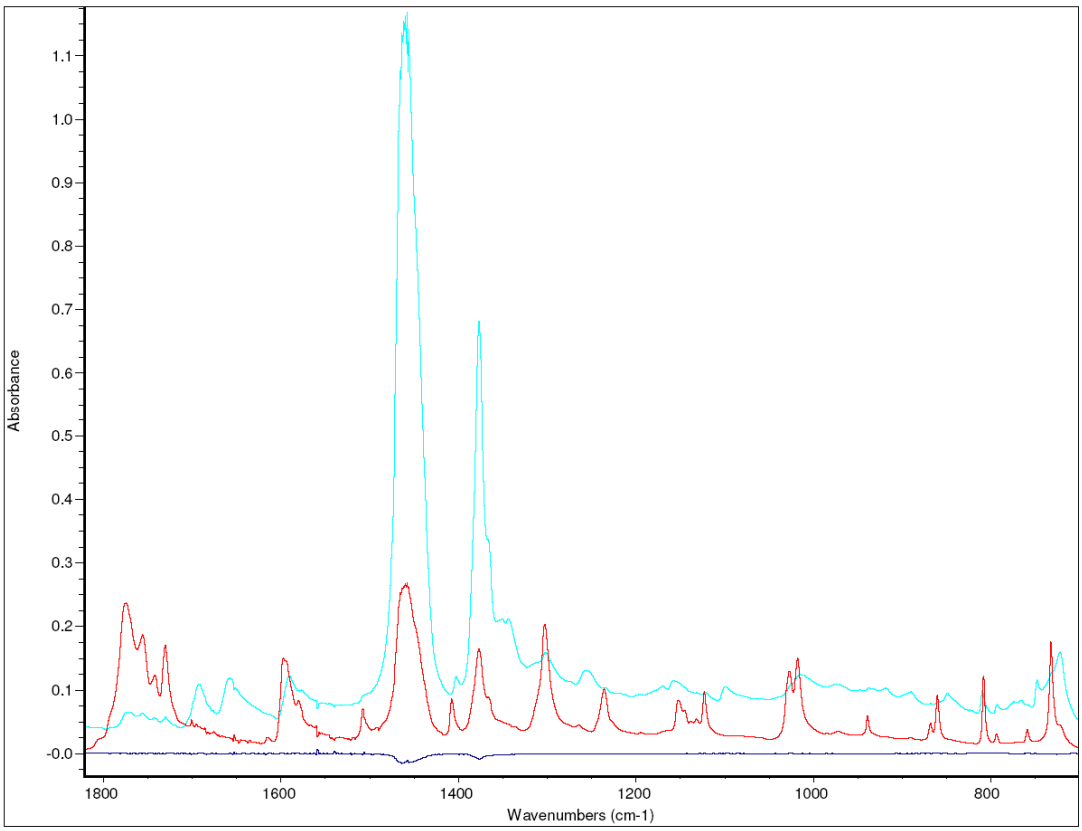

Figure 2.2.14: IR spectra of PTCDA, pPDI

Elemental Analysis:

Samples of pPDI were sent to Galbraith Laboratories for elemental analysis. C, H, N, and P were analyzed. The results are summarized below in Table 2.2.1. Carbon and hydrogen analyses closely match theoretical calculations of bis-pPDI. However, the nitrogen and phosphorus analysis differ considerably. To attempt to account for this, theoretical mass calculations were made for both mono-pPDI and PDI. These are included in Table 2.2.2.

Table 2.2.2: Calculated & experimental mass analyses

Element	bis-pPDI (calc.)	mono-pPDI (calc.)	PDI (calc.)	Galbraith
C	56.79%	63.17%	73.85	56.58%
H	3.81%	3.14%	2.58	3.89%
N	4.41%	2.73%	7.18	9.47%
P	9.76%	6.03%	0.00	5.92%

2.3 Sensitization of Titania Electrodes with pPDI

Titania electrodes were submersed in a neutral solution of pPDI dye (20 μM) for 24 h. Upon removal, they were washed with deionized water and dried. A UV-vis spectrum of 20 μM pPDI in deionized water is shown below in Figure 2.3.1.

Ultraviolet-visible light spectrometry (UV-vis):

Figures 2.3.2 through 2.3.5 below show pictures of substrates through different stages of development; a blank FTO substrate, a plain underlying layer of dense titania, a thick porous layer of titania, and a dye-sensitized porous titania layer. Corresponding UV-vis spectra are shown in Figure 2.3.6.

Spectra of a plain FTO substrate (shown in dark blue) compared with a substrate with a single sintered layer of Sol A (shown in red) show little additional absorbance due to the dense, blocking layer of the titania, demonstrating very high transparency.

The higher absorbance measured for both sensitized (Ti4.2 pPDI, Ti4.3 pPDI) and unsensitized substrates (Ti4.4, Ti4.5) also demonstrate higher light scattering and internal reflectance of the thick, porous layers. Additional absorbance due to the pPDI sensitizer is negligible. UV-vis measurements of electrode Ti4.0 were taken both before and after sensitization, the graph of the results is shown in Figure 2.3.7. Again, additional absorbance due to adsorbed sensitizer is negligible.

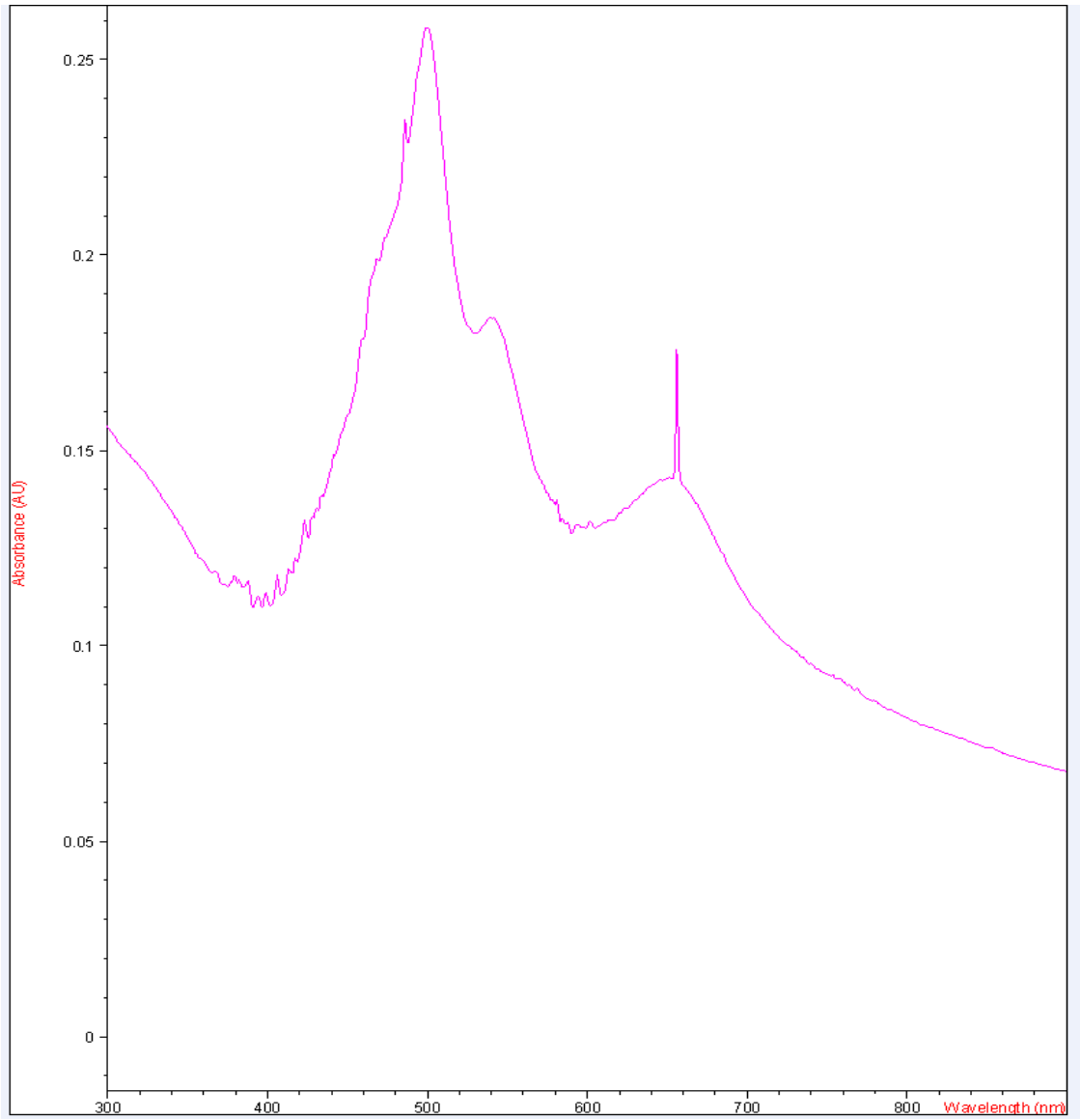

Figure 2.3.1: UV-vis absorption spectrum of a 20 µM solution of pPDI

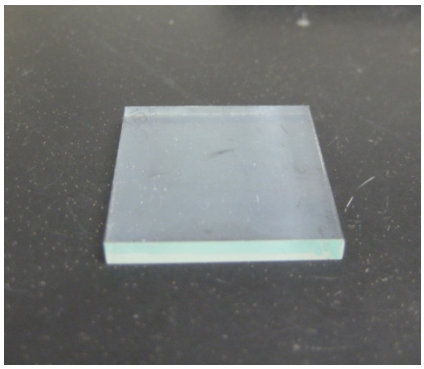

Figure 2.3.2: A plain FTO substrate

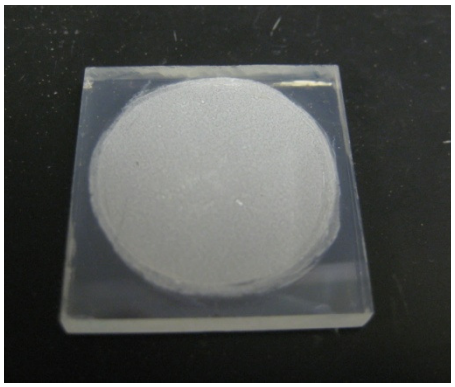

Figure 2.3.4: An unsensitized, thick layer of titania

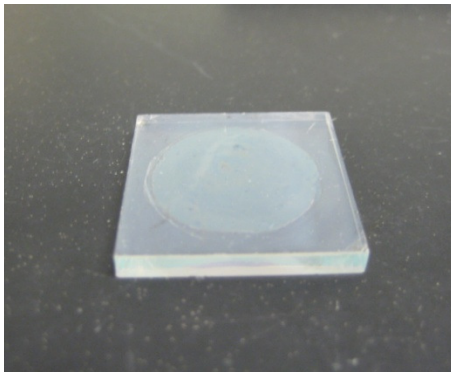

Figure 2.3.3: An unsensitized, thin layer of titania

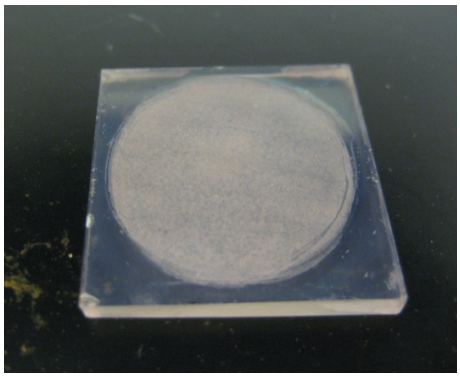

Figure 2.3.5: A sensitized, thick layer of titania

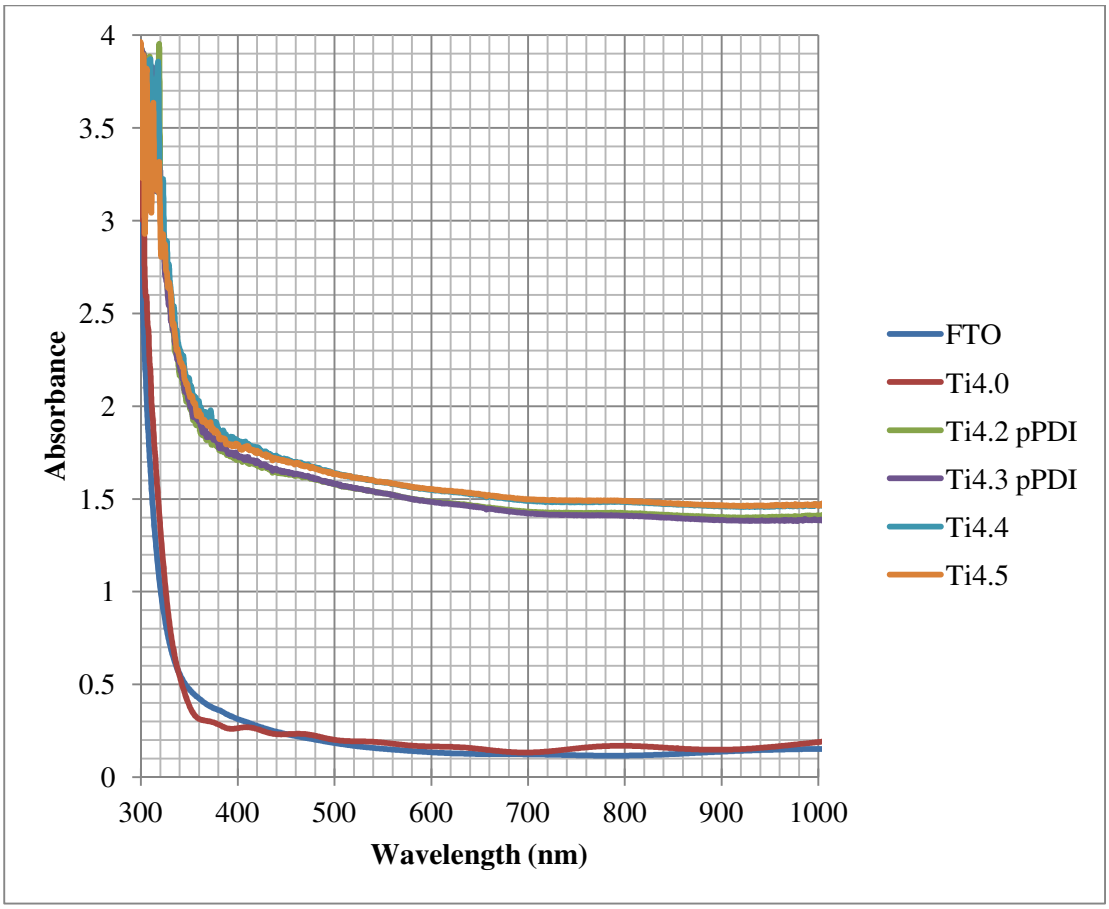

Figure 2.3.6: UV-vis spectra of select electrodes:
Plain FTO substrate; dense TiO_2 (Ti4.0); porous TiO_2(Ti4.4, Ti4.5);
and porous, sensitized TiO_2 (Ti4.2pPDI, Ti4.3ppDI)

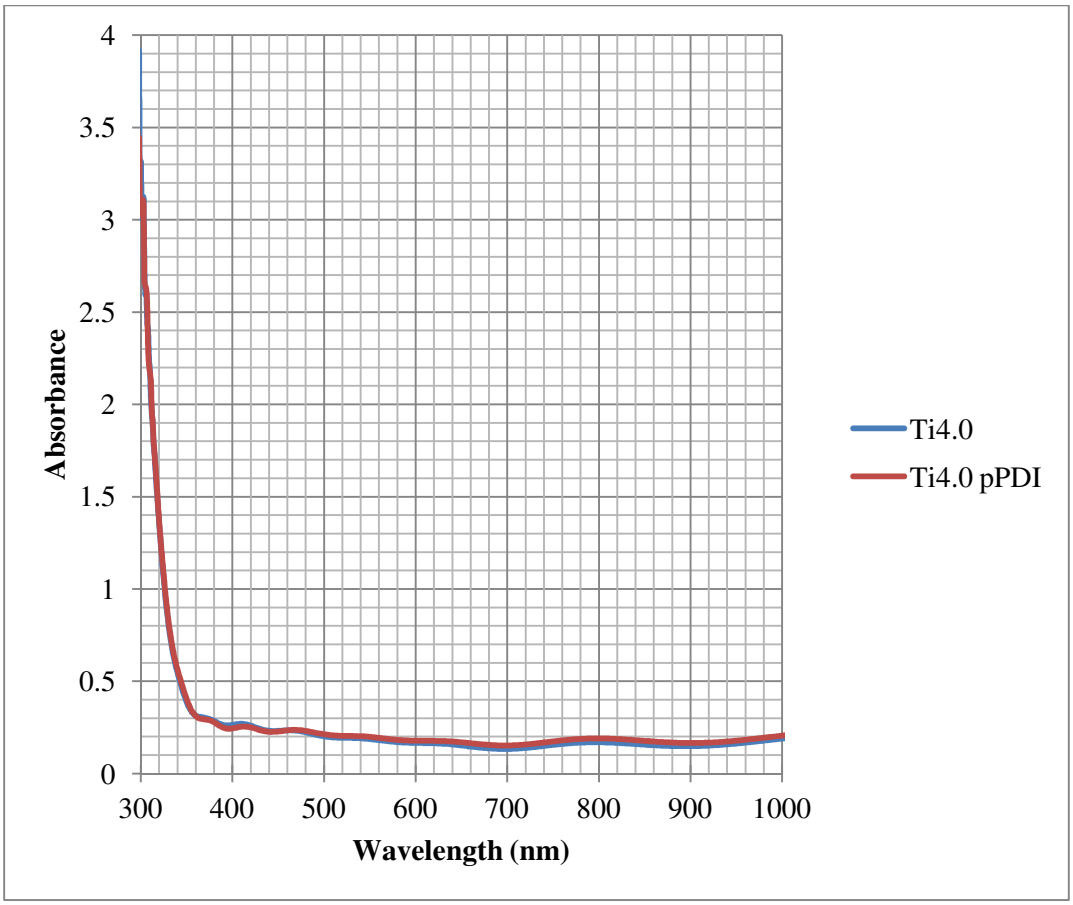

Figure 2.3.7: Electrode Ti4.0, before and after sensitization with pPDI

Electrochemical Characterization of Sensitized Electrodes:

Figure 2.3.8 below shows the components of the electrochemical cell used to characterize various electrodes. In the first row (left to right) are the PTFE cell body, Ag/AgCl reference electrode, Pt counter electrode (2.4 cm^2); in the second row (left to right) are the quartz window, a representative substrate (plain FTO), and the brass working electrode contact. The photo of the cell, assembled and connected, is shown in Figure 2.3.9.

Cyclic voltammetry (CV) measurements were carried out on a PAR potentiostat/galvanostat, Model 273A. Light/dark experiments were illuminated with a Newport Model 66921 horizontal Xe-arc lamp at 500 W. Optical filters (2"×2", Newport) were placed between the light source and the cell to remove both IR and UV portions of the light source, leaving only visible light to illuminate the cell. A light spectrum of the IR absorber in series with the 400 nm long-pass cutoff filter is shown below in Figure 2.3.10. The low absorbance of the filter between 400 and 700 nm is the visible spectrum that is transmitted to illuminate the cell.

Unless otherwise stated, light dark experiments were performed with IR and UV filtered light. Unfiltered experiments are denoted “UF-light”. A photo of the cell placed in the light rail assembly, including filters, is shown below in Figure 2.3.11.

All electrochemical measurements were performed using a Ag/AgCl electrode. All graphs are referenced to this potential, +0.222 V vs. NHE.

Figure 2.3.8: Cell components with side view of cell body

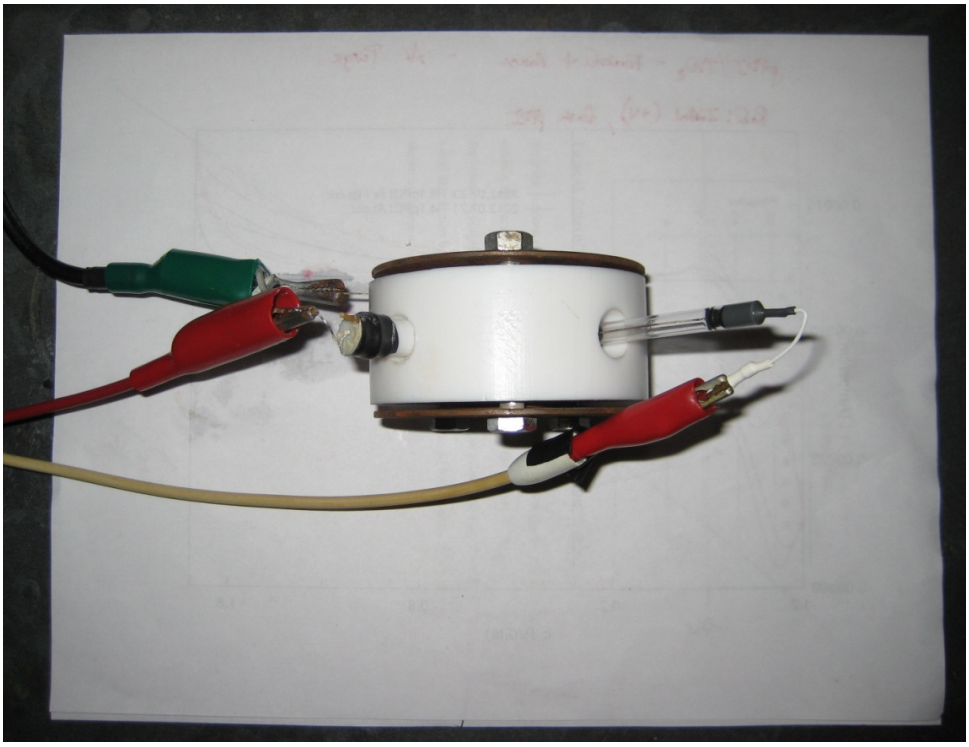

Figure 2.3.9: Cell assembly, top view

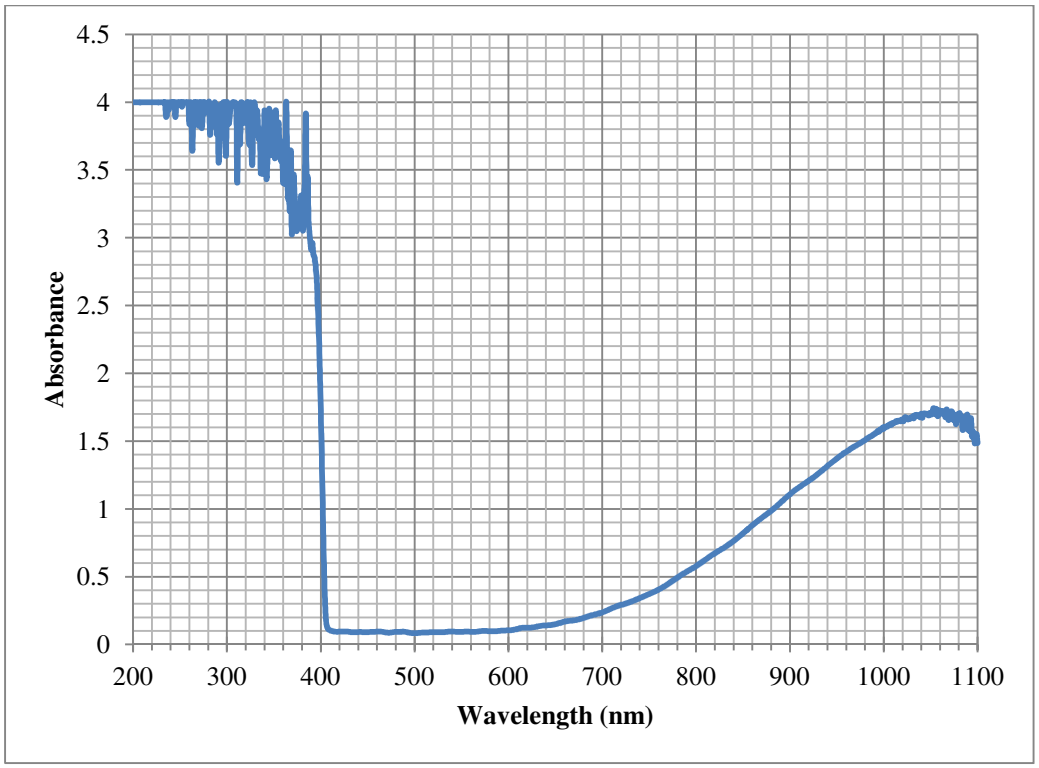

Figure 2.3.10: UV-vis spectrum of optical filters

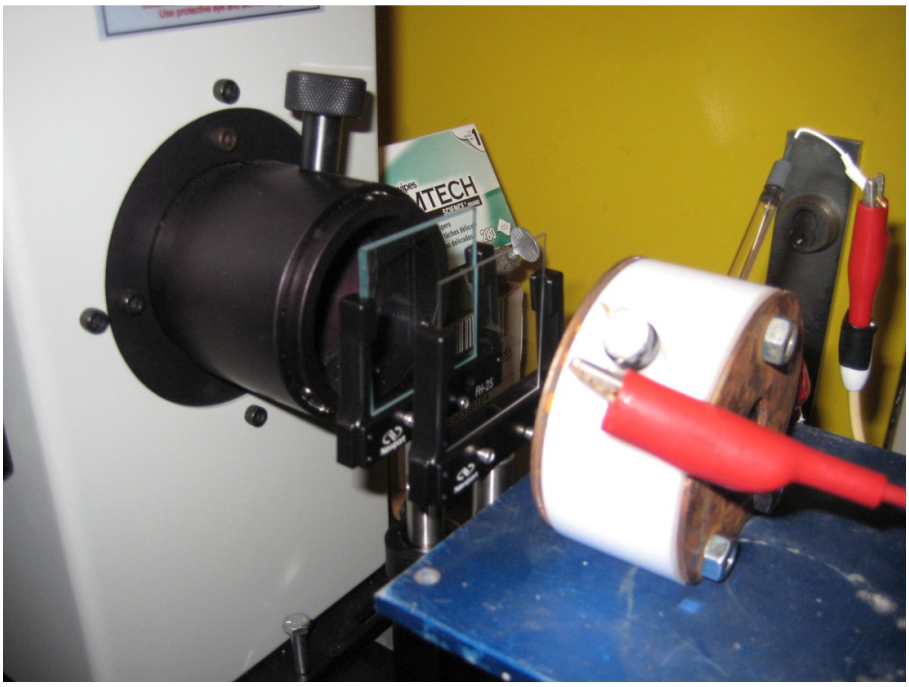

Figure 2.3.11: Light rail assembly with filters

CVs of a plain FTO substrate are shown below in Figure 2.3.12 (negative initial sweep; 0.1 M KOH). The anodic and cathodic currents seen at 0.8 V and -0.6 V correspond to the oxidation and reduction of water. The CV was repeated while illuminated with unfiltered light (black trace) to demonstrate the FTO layer's lack of photoactivity, even with UV light present.

CVs of a porous titania substrate under dark, filtered light, and unfiltered light conditions are shown below in Figure 2.3.13 (initial sweep; 0.1 M KNO3). Titania is very active with UV light; even at reducing potentials out to 0.3 V, titania is capable of water oxidation. It is essential to filter out the UV component of our light source to demonstrate any visible light sensitization of the titania due to adsorbed dye.

Non-aqueous CVs of a titania electrode were taken in distilled acetonitrile (MeCN) with 0.1 M recrystallized tetraethylammonium perchlorate (TEAP) with a positive initial sweep (0 V > 2.0 V > -1.2 V > 0 V). Figures 2.3.14 and 2.3.15 show CVs of a porous titania electrode before and after sensitization with pPDI (TEAP/MeCN).

A multiple cycle CV demonstrating the irreversible activity seen in both Figure 2.3.14 and Figure 2.3.15 is shown in Figure 2.3.16 (0 V → 2.0 V → -0.9 V → 0 V; 10 cycles; positive initial sweep; TEAP/MeCN). The redox couple seen in Figure 2.3.15 was also cycled; CV is shown in Figure 2.3 (0 V → 0.1 V → -1.2 V → 0 V; 100 cycles; positive initial sweep; TEAP/MeCN).

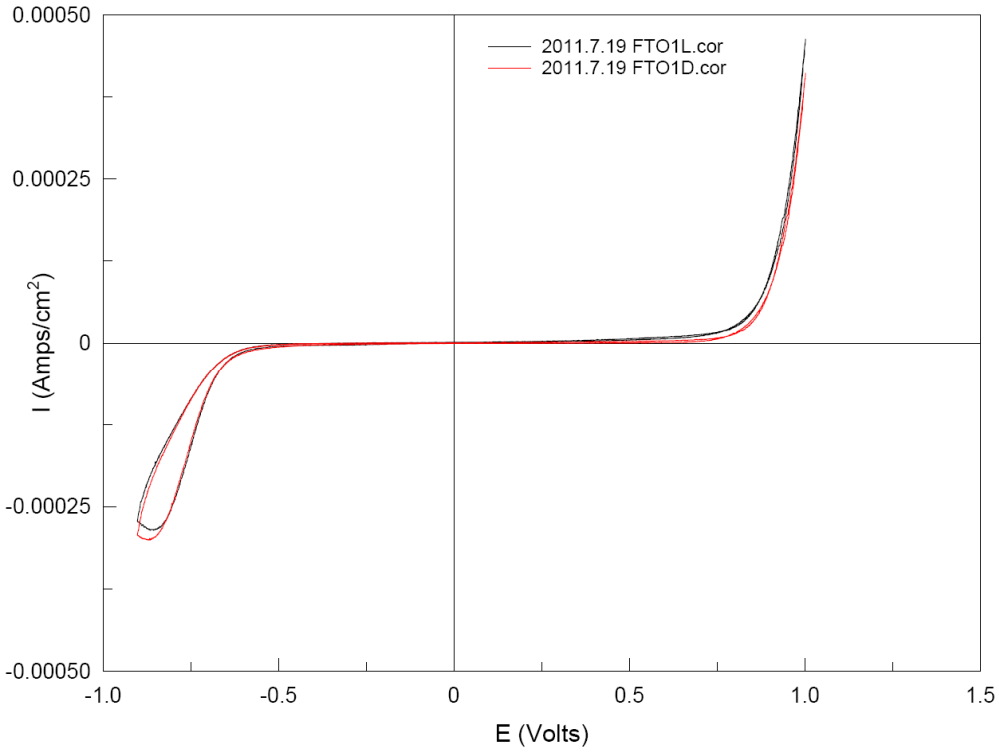

Figure 2.3.12: UF-light/Dark CVs of plain FTO substrates

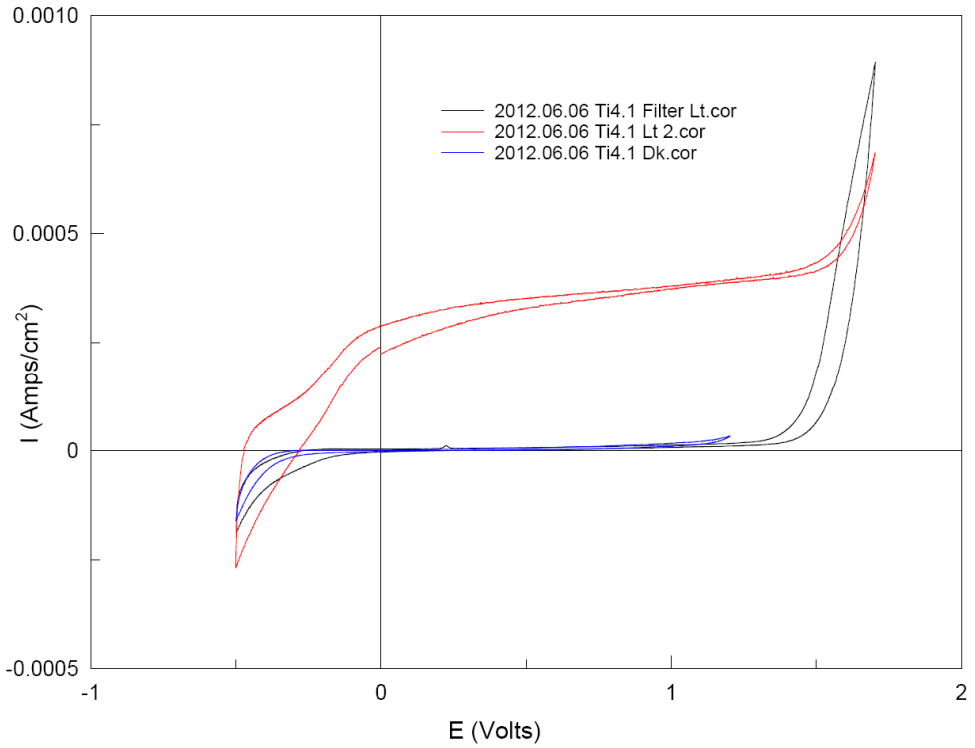

Figure 2.3.13: UF-light/light/dark CVs of a porous titania electrode

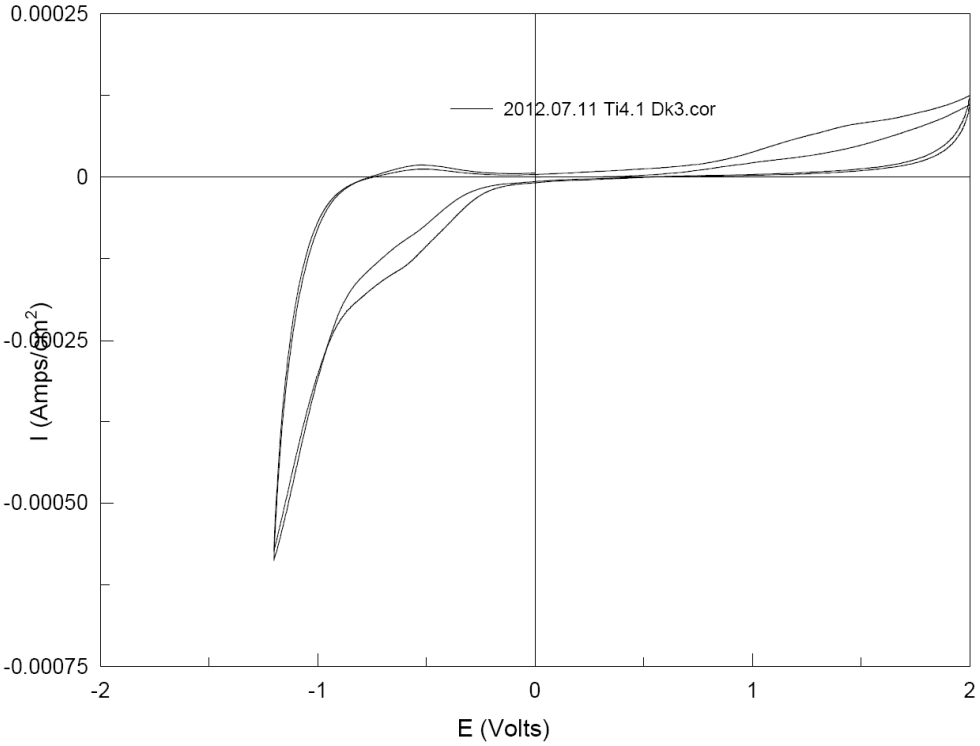

Figure 2.3.14: CV of a porous titania electrode Ti4.1 (pre-sensitization);
oxidation/reduction of electrolyte system seen at 1.4 V & -0.5 V

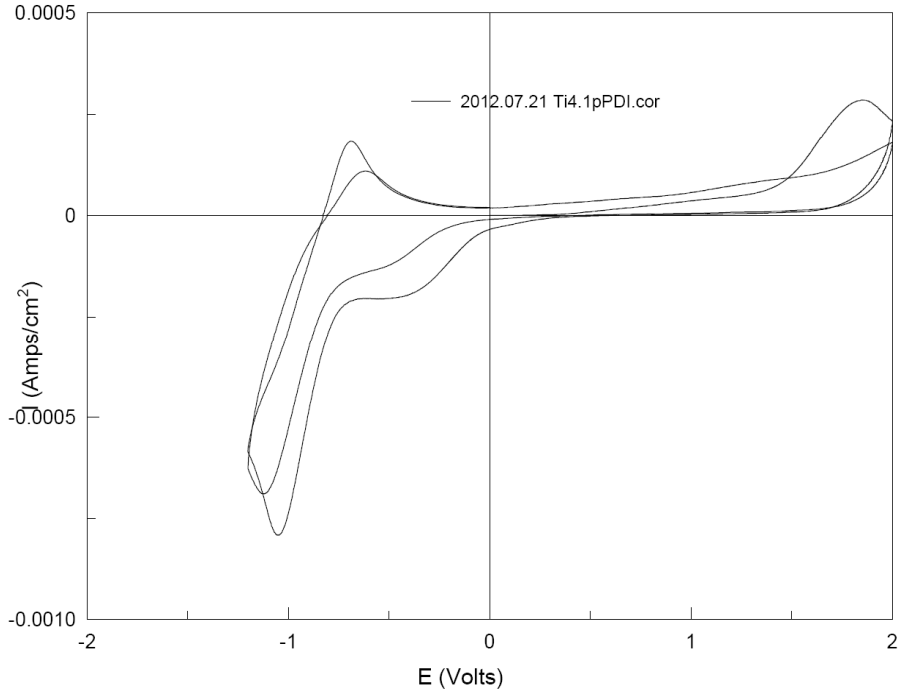

Figure 2.3.15: CV of a porous titania electrode Ti4.1pPDI (post-sensitization) showing oxidation of electrolyte system seen at 1.4 V & -0.4 V and reversible redox couple at -0.7 V & -1.1 V

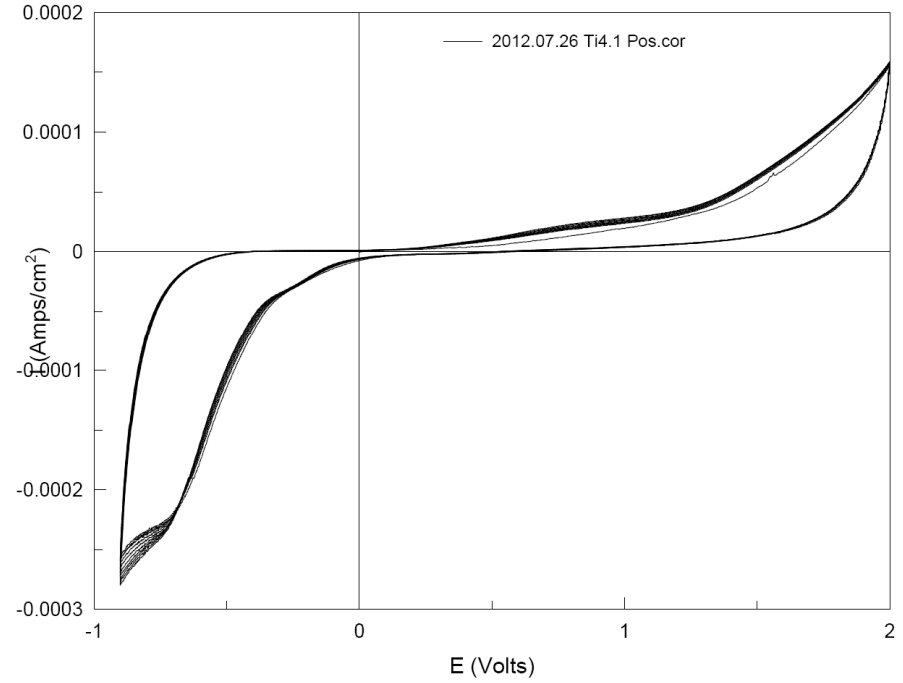

Figure 2.3.16: 10-cycle CV of electrolyte oxidation/reduction (Ti4.1pPDI)

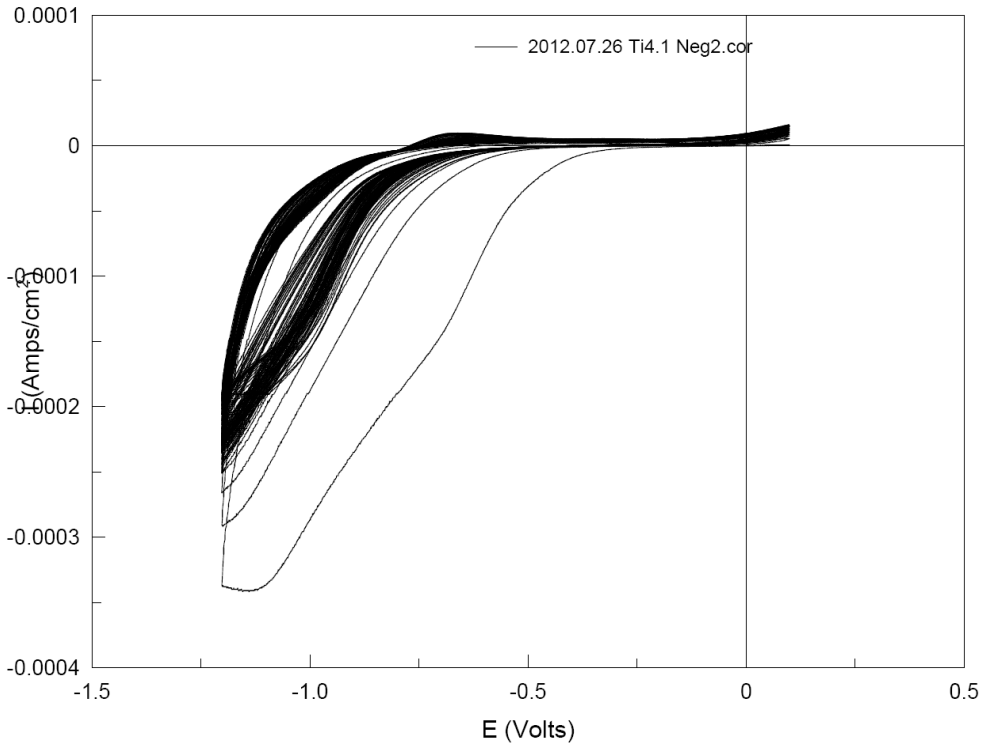

Figure 2.3.17: 100-cycle CV of the pPDI redox couple (Ti4.1pPDI)

Potentiostatic experiments (PS) were carried out to test whether or not the pPDI sensitized electrodes were capable of a sustained oxidation of a reduced species, ferrocyanide, under illumination. Light/dark CVs were carried out on a stock solution of potassium ferrocyanide (1 mM in 0.1 M KOH) with an unsensitized titania electrode to determine the location of the oxidation potential of the species; see Figure 2.3.18. As seen in the CVs, the E_{ox} of ferrocyanide occurs at 0.31 V. A small light bias is seen such that $E_{ox, light}$ occurs at a slightly lower potential of 0.30 V. The cell for subsequent PSs was biased at 0.25 V potential, just below the E_{ox} of ferrocyanide; this enables facile oxidation of the species.

A series of experiments were carried out with different filters to observe any light enhanced oxidation due to the pPDI sensitizer. The duration of the PSs was 60 s; the light source was powered on to illuminate the cell at the midpoint of each experiment. Figure 2.3.19 shows PSs of both electrodes Ti4.5 (unsensitized) and Ti4.3pPDI (sensitized) with long-pass cutoff filters at 400 nm, 455 nm, and 590 nm. The results are summarized below in Table 2.3.1.

Table 2.3.1: Summary of potentiostatic experiments

Cutoff Filter	Max Current (µA), Ti4.5	Max Current (µA), Ti4.3pPDI
None	99	37
400 nm	18	5
455 nm	11	5
590 nm	1	1

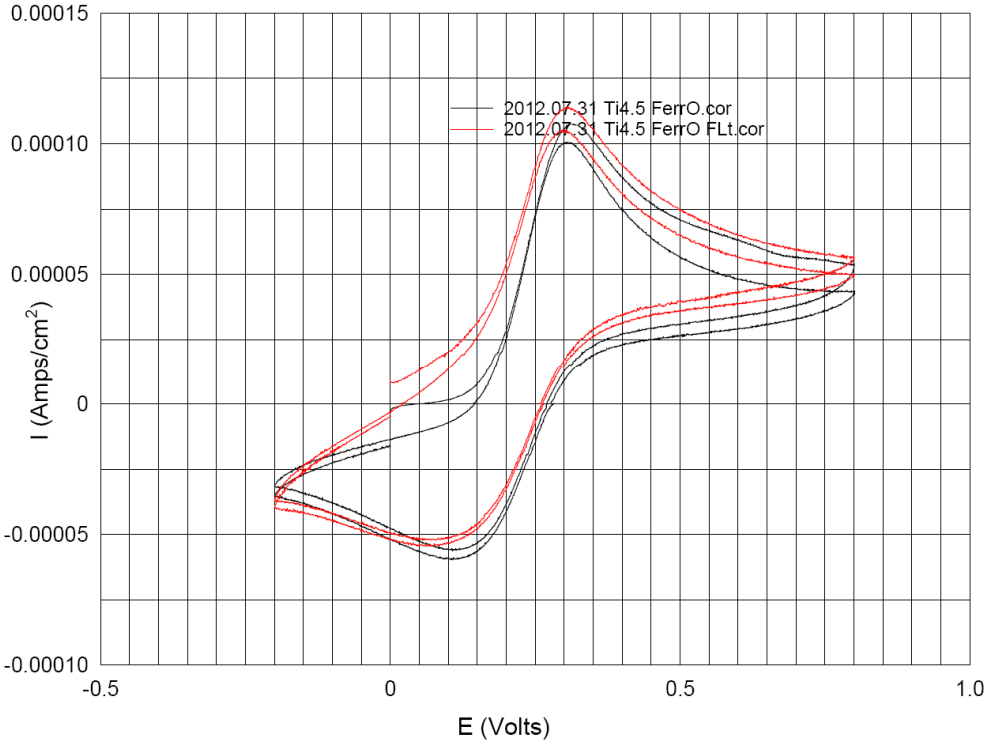

Figure 2.3.18: Light/dark CVs of ferrocyanide

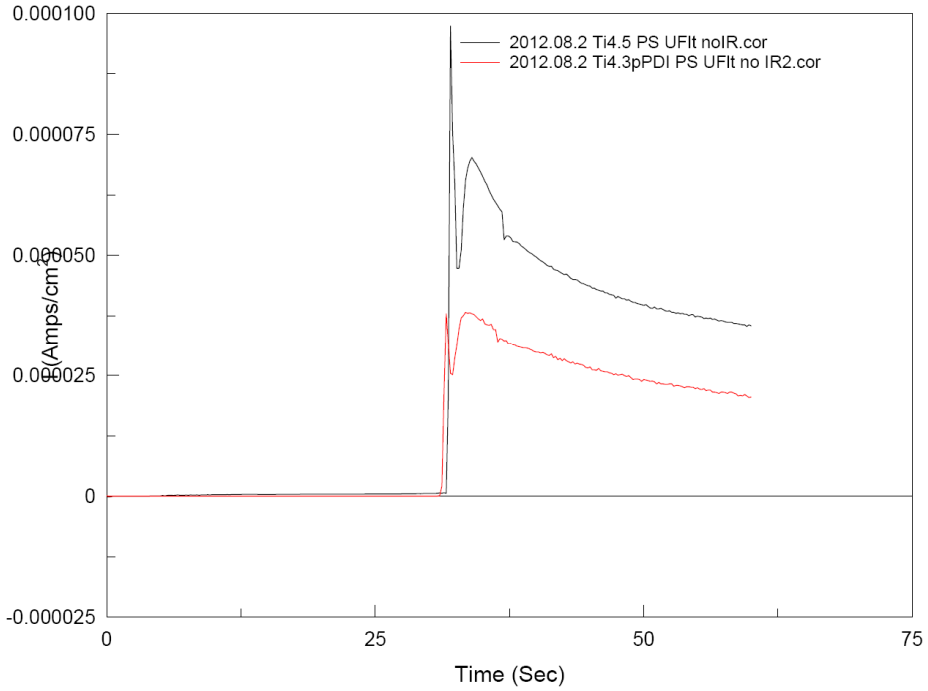

Figure 2.3.19: PSs of unsensitized TiO_2 (black) and sensitized (red) with unfiltered light

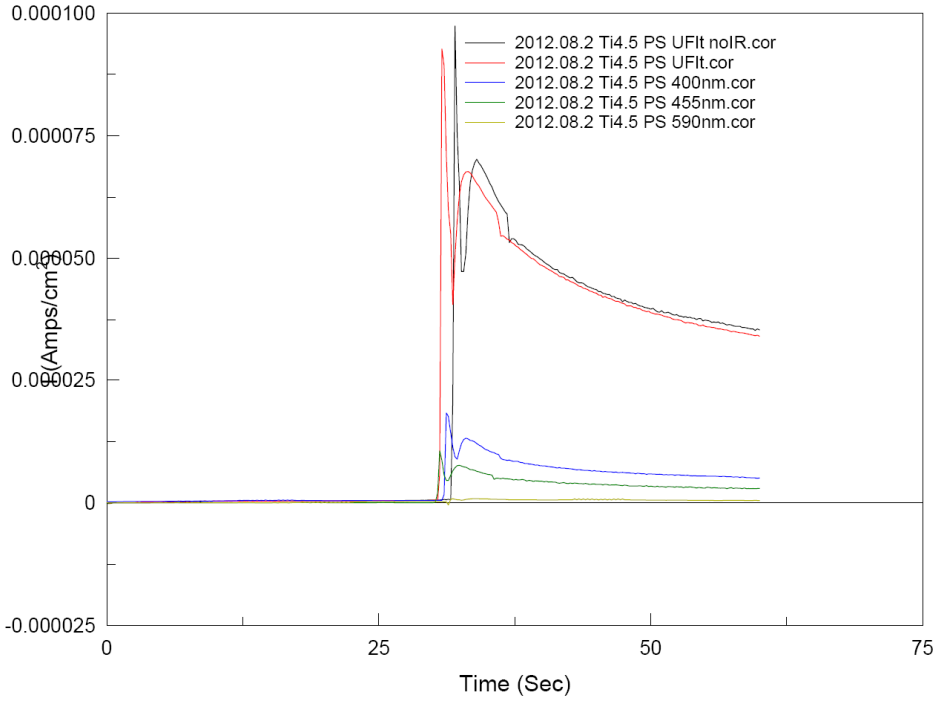

Figure 2.3.20: PSs of unsensitized TiO_2 with various cutoff filters

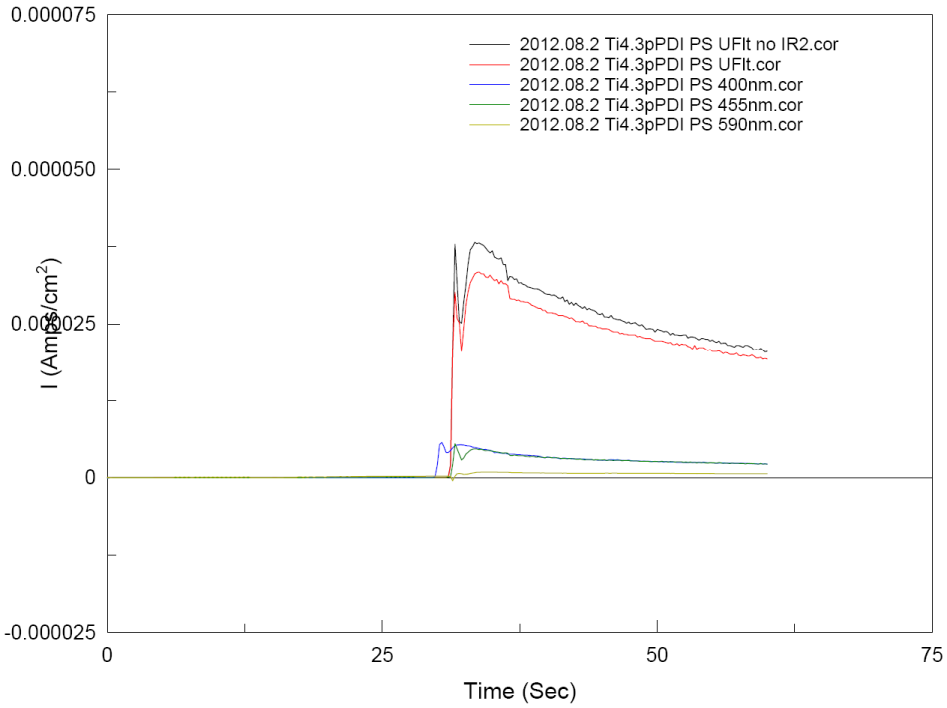

Figure 2.3.21: PSs of sensitized TiO_2 with various cutoff filters

CHAPTER 3

Discussion of Experimental Results

2.1

Creation of high surface area electrodes for dye sensitization is desirable because it enables more adsorbed dye to be exposed to the cell environment. This allows for greater light absorption and should yield improved photoelectrochemical activity. The SEM images described above demonstrate the much improved electrode surface of the porous titania electrodes compared with the dense, flat electrode.

2.2

NMR:

In the 3-APPA ^{1}H spectrum, the protons adjacent to the amine lie at 3.06 ppm. After the reaction, shown in the ^{1}H spectrum of pPDI, this signal is shifted to 3.9 ppm indicating insertion into the electron rich carboximide structure. A residual triplet lies very near the original amine signal at 3.09 ppm. This residual peak was integrated with respect to the large signal at 3.9 ppm and a value of 0.0158 was obtained. This suggests the presence of the reagent 3-APPA at 1.6% concentration versus the product. Proton exchange between the phosphonic acid and the solvent led to the enormous water peak near 4.8 ppm. A small signal due to the acidic protons is seen at 8.7 ppm.

The ^{31}P spectrum of pPDI shows a lone singlet at 24.8 ppm. This shift from the 3-APPA peak of 23.7 ppm suggests that the electronic environment of all phosphonic acid moieties has been altered, namely, by attachment to the perylene structure. These ^{31}P shifts are consistent with shifts of alkylphosphonic acid moieties in the literature.[21,22,23]

The authentic ^{13}C spectrum of PTCDA consists of a single peak at 160 ppm and a group of 6 peaks between 115 and 135 ppm (at approx. 117, 124, 127, 128, and 135 ppm). Apparent peaks outside of this range are, in fact, spinning sidebands due to the large field anisotropies generated by spinning the flat, sp^2 hybridized carbons in the solid state. For example, the peaks at 80 and 240 ppm are side bands of the authentic peak at 160 (±80 ppm). The lone peak at 160 ppm, farthest downfield is due to the carbonyl group (carbon #7 in Figure 2.2.11). The aromatic carbons (#1-6) are grouped tightly together between 115 and 135 ppm, making peak assignment difficult. Carbons 1 and 2, with only two equivalent carbons each, are expected to have short peaks, relative to the remaining five carbons with four equivalents. Thus, we can deduce the two shoulders on either side of the more prominent peak at 127 ppm are likely carbons 1 and 2. Relative to the other aromatic carbons, carbons 4 and 5 are expected to have the larger peaks due to the attached hydrogens. These are thus expected to be the peaks at 116 and 135 ppm. The extra height of the peak at 135 ppm is supposed to be due to overlap with carbon 3.

The solid ^{13}C spectrum of pPDI presents problems for interpretation. The seven peaks in the aromatic region indicate more than one species present in the sample. Further complicating interpretation is the absence of spinning sidebands of the flat, sp^2 aromatic carbons which are clearly present in the PTCDA spectrum. The three peaks in the alkyl region, at 25 and 28 ppm, are expected to be from the carbons α and β, respectively, from the phosphonic acid group. The peak at 41 ppm is γ to the phosphonic acid; it more deshielded being next to the electron rich perylene structure. Described as R-CH_2-X, its broad baseline likely arises from a variation in how it is bound to the perylene core (i.e. X may correspond to a dicarboximide, carboximide, or unreacted anhydride site). The 5 signals between 160 and 180 suggest 5 different combinations of the aforementioned species surrounding the carbonyl sites. The small, poorly resolved signals above 200 ppm suggest the presence of unknown aldehyde and/or ketone configurations.

IR:

Dips in the baseline between 1465-1450, 1380-1370 cm^{-1} (also 2950-2800 cm^{-1}, not shown) are from the alkyl stretches of the Nujol oil itself. Very high absorbance in these regions due to the Nujol renders data from subsequent spectra unreliable due to the very low about of reference light transmitted.

The strong anhydride signal in the PTCDA spectrum from 1720-1800 cm^{-1} is largely eliminated in the pPDI spectrum. Amide signals at 1660 and 1690 cm^{-1}, absent for PTCDA, are clearly present in the pPDI spectrum. Although the pPDI spectrum displays much larger relative absorbance in the aliphatic regions (1465-1450, 1380-1370 cm^{-1}) than PTCDA, presumably due to the alkylphosphonic acid moieties, this data is dubious due to the tenable baseline in those regions. Just beyond this range, from 1345 to 1355 cm^{-1}, large absorbance in the pPDI spectrum are again due to the amide group.

Elemental Analysis:

Appreciable amounts of either mono-pPDI or PDI in the powder sample could account for the low P result. The high nitrogen measurement could perhaps be explained by significant amounts of the 3-APPA reagent; however, much higher phosphorus measurements would also be expected.

2.3

The UF-light/dark CVs of the plain FTO substrate in Figure 2.3.12 demonstrates the negligible photoactivity of the underlying FTO substrates used for fabrication of titania electrodes. The UF-light CV (in black) and the dark CV (in red) closely retrace each other. The currents measured at $E > 0.75$ V and at $E < -0.6$ V are due to oxidation and reduction of water under basic conditions. Figure 2.3.13 shows CV's of a porous titania electrode under neutral aqueous conditions. In the dark (CV shown in blue), we see a cathodic wave, corresponding to the onset of water reduction, at $E < -0.3$ V. The CV of titania illuminated with filtered light (shown in black) closely matches that of the

dark CV; reduction at E < -0.3 V and oxidation at E > 1.4 V.

Exposing the titania to unfiltered light, with an appreciable UV component, results in dramatically different electrochemical properties. The 3.2 eV bandgap of titania renders it active upon exposure to UV light. A UF-light CV (shown in red) was carried out and demonstrates this UV activity. Even upon the initial negative sweep, and out to -0.3 V, the titania is capable of water oxidation. Filtration of the light source, especially the UV portion, is critical to assessing the performance of the pPDI sensitizer. Any activity of the dye resulting from illumination with UV light could be confused with the photoactivity of the titania.

Non-aqueous CVs of a titania electrode were taken in distilled acetonitrile (MeCN) with 0.1 M recrystallized tetraethylammonium perchlorate (TEAP) with a positive initial sweep (0 V > 2.0 V > -1.2 V > 0 V). This was done to provide a wide electrochemical window for redox characterization of the dye; see Figure 2.3.14 for representative CVs of electrode Ti4.1. This electrode was then sensitized with pPDI; the CV experiment was then repeated (shown in Figure 2.3.15).

Irreversible redox activity is apparent for the pre-sensitized electrode at E < -0.5 V and E > 1.0 V this is likely due to oxidation/reduction of the electrolyte solution. However, after sensitization, a reversible redox couple emerges at E = -1.1 V and E = -0.7 V. Farther investigation of these couples was done to elucidate this activity. The CV boundaries were then set to straddle the irreversible activity (0 V > 2.0 V > -0.9 V > 0 V); ten cycles were performed (Figure 2.3.16). The following CV in Figure 2.3.17 represents an attempt to lock in to the reversible couple seen in Figure 2.3.15; 100 cycles were performed. The reversible reduction of the dye suggests transfer of electrons from the titania to the dye.

The PSs clearly show diminished oxidative currents when either the 400 or 455 nm cutoff filters are used. With the 590 nm cutoff filter in place, an oxidative current is nearly immeasurable (~1 μA) for both the sensitized and unsensitized electrodes. With the IR absorber and the 590 nm cutoff both in place, very little light is transmitted to the cell. The fact that the pPDI sensitizer is stifling electron flow to the anode tells us that electron transfer to the titania layer is being inhibited rather than enhanced. Adding to the fact that transfer of electrons to the dye from the titania is facile, this suggests an energy band mismatch of the two materials.

CHAPTER 4

Conclusions

The creation of enhanced surface area titania electrodes was indeed achieved. Preparation of electrodes in this way could be further optimized for even higher surface area; however, this was not the ultimate focus of the research.

The very poor solubility of pPDI made purification via liquid chromatography impossible. Simple filtration of the reaction product is all that could be done to remove the reagent 3-APPA and imidazole. It is likely that traces of these compounds remain; especially imidazole as its tendency to hydrogen bond might have left species bound to pPDI. This also would partly explain the high nitrogen content measured with elemental analysis. The presence of 3-APPA is evident from the ^{1}H NMR spectra. Inability to perform LC also inhibits preparatory separation of the different reaction products (i.e. bis-pPDI, mono-pPDI, anhydride/carboximide conformations, amide/carboxylic acid conformations). This prevents crystallographic characterization and likely complicates electrochemical characterization.

Nonetheless, having continued with multiple attempts to characterize the dye, we are left with much evidence that suggests that bis-pPDI is at least a major product of the reaction. We are also left to conclude that there are very likely other soluble perylene species in the reaction product. The electrophoretic experiment points to a uniform mass to charge ratio of the dye sample. This result, initially very promising, remains enigmatic in light of the additional characterization.

Reversible oxidation was not seen in the anodic CV regions. However, a reversible reduction of the dye is apparent. The corroboratory PS data indicates electron transfer from the titania to the dye is more favored. This indicates the reduction potential of pPDI is actually higher (less negative) than the conduction band of the titania. This situation is antagonistic to the water splitting scheme described in Figure 1.2. Other dyes could be studied with titania that possess a more favorable arrangement of their reduction potentials. Also, different semiconductor materials could be studied with pPDI such that their conduction band is higher (less negative) than the reduction potential of pPDI to encourage oxidative transfer of electrons from the dye.

Recommendations for further research:

Already mentioned were the possibilities of pairing different materials for use the in water splitting scheme; different dyes ought to be studied with titania and different semiconductors could be used for sensitization with pPDI. The fabrication of titania 'nanotubes' for use as a photoanode could provide even higher surface area for dye adsorption and perhaps ought to be used in lieu of the mesoporous structure.

The solubility challenges of pPDI warrant different synthetic approaches for perylene derivatives. Longer alkylphosphonic acid chains for use as the solubilizing and linkage agent could be used; 6-aminohexylphosphonic acid, for example, is commercially available. Modification of the 'bay' positions (where the aromatic H atoms lie on the perylene structure) with halides have shown to significantly increase the solubility of perylenes. This could also be investigated to enhance solubility of any future perylene derivatives.

References

1. Thompson, L. G. Climate Change: The Evidence and Our Options. *The Behavior Analyst*. **2010**, *33*, 153-170.

2. Rifkin, J. *The Hydrogen Economy*; Jeremy P. Tarcher/Putnam: New York, 2002; Chapter 8.

3. Bartok, Jr., J., W. "Approximate Heating Values of Common Fuels"; University of Connecticut: Storrs, CT, 2004.

4. Thomas, G. "Overview of Storage Development DOE Hydrogen Program"; Hydrogen Program Review; Sandia National Laboratories, Livermore, CA, 2000.

5. http://www.engineeringtoolbox.com/co2-emission-fuels-d_1085.html Combustion Fuels - Carbon Dioxide Emission

6. U.S. Energy Information Administration. The Impact of Increased Use of Hydrogen on Petroleum Consumption and Carbon Dioxide Emissions: Existing Hydrogen Production Capacity. http://eia.gov/oiaf/servicerpt/hydro/appendixc.html (accessed Apr 30, 2012).

7. Hoffmann, P. *Tomorrow's Energy*; MIT Press: Cambridge, MA, 2001; Chapter 4.

8. Pearsall, N. *A Strategic Research Agenda for Photovoltaic Solar Energy Technology*; DG JRC – Institute for Energy; The European Commission: Ispra, Italy, 2011.

9. Roes, A., L.; Alsema, E., A.; Blok, K.; Patel, M., K. Ex-ante Environmental and Economic Evaluation of Polymer Photovoltaics. *Prog. Photovolt: Res. Appl.* **2009**, *17*, 373-393.

10. Hagfeldt, A.; Boschloo, G.; Sun, L.; Kloo, L.; Pettersson, H. Dye-Sensitized Solar Cells. *Chem. Rev.* **2010**, *110*, 6595-6663.

11. Hashimoto, K.; Irie, H.; Fujishima, A. TiO_2 Photocatalysis: A Historical Overview and Future Prospects. *Jpn. J. Appl. Phys.* **2005**, *44*, 8269-8285.

12. Walter, M., G.; Warren, E., L.; McKone, J., R.; Boettcher, S., W.; Mi, Q.; Santori, E., A.; Lewis, N., S. Water Splitting Cells. *Chem. Rev.* **2010**, *110*, 6446-6473.

13. Youngblood, W., J.; Lee, S., A.; Kobayahsi, Y.; Hernandez-Pagan, E., A.; Hoertz, P., G.; Moore, T., A.; Moore, A., L.; Gust, D.; Mallouk, T., E. Photoassisted Overall Water Splitting in a Visible Light-Absorbing Dye-Sensitized Photoelectrochemical Cell. *J. Am. Chem. Soc.* **2009**, *131*, 926-927.

14. Park, H.; Bae, E.; Lee, J.; Park, J.; Choi, W. Effect of the Anchoring Group in Ru-Bipyridyl sensitizers on the Photoelectrohemical Behavior of Dye-Sensitized TiO_2 Electrodes: Carboxylate versus Phosphonate Linkages. *J. Phys. Chem. B* **2006**, *110*, 8740-8749.

15. Youngblood, W., J.; Lee, S., A.; Kobayahsi, Y.; Hernandez-Pagan, E., A.; Hoertz, P., G.; Moore, T., A.; Moore, A., L.; Gust, D.; Mallouk, T., E. Photoassisted Overall Water Splitting in a Visible Light-Absorbing Dye-Sensitized Photoelectrochemical Cell. *J. Am. Chem. Soc.* **2009**, *131*, 926-927.

16. Yukruk, F.; Dogan, A., L.; Canpinar, H.; Guc, D.; Akkaya, E., U. Water-Soluble Green Perylenediimide (PDI) Dyes as Potential Sensitizers for Photodynamic Therapy. *Org. Lett.* **2005**, *7*, 2885-2887.

17. Ernstorfer, R.; Gundlach, L.; Felber, S.; Storck, W.; Eichberger, R.; Willig, F. Role of Molecular Anchor Groups in Molecule-to-Semiconductor Electron Transfer. *J. Phys. Chem. B* **2006**, *110*, 25383-25391.

18. Yella, A.; Lee, H.; Tsao, H., N.; Yi, C.; Chandiran, A., K.; Nazeeruddin, M., K.; Diau, E., W.; Yeh, C.; Zakeeruddin, S., M.; Gratzel, M. Porphyrin-Sensitized Solar Cells with Cobalt (II/III)-Based Redox Electrolyte Exceed 12 Percent Efficiency. *Science*. **2011**, *334*, 629-633.

19. Youngblood, W., J.; Lee, S., A.; Maeda, K.; Mallouk, T., E. Visible Light Water Splitting Using Dye-Sensitized Oxide Semiconductors. *Acc. Chem. Res.* **2009**, *42*, 1966-1973.

20. Wang, C.-T.; Yen, C.-F. Titania nanocomposite thin films with enhanced photovoltaic efficiency: Effects of Ti-alkoxide sol and compact layer. *Surf. Coat. Technol.* **2012**, *206*, 2622-2627.

21. Martinson, A., B., F.; Massari, A., M.; Joong Lee, S.; Gurney, R., W.; Splan, K., E.; Hupp, J., T.; Nguyen, S., T. Organic Photovoltaics Interdigitated on the Molecular Scale. *J. Electrochem. Soc.* **2006**, *153*, A527-A532.

22. Kern, J., T.; Kerwin, S., M. The Aggregation and G-Quadruplex DNA Selectivity of Charged 3,4,9,20-perylenetetracarboxylic Acid Diimides. *Bioorg. Med. Chem. Lett.* **2002**, *12*, 3395-3398.

23. Tuesuwan, B., T.; Kern, J., T.; Thomas, P., W.; Rodriguez, M.; Li, J.; David, W., M.; Kerwin, S., M. Simian Virus 40 Large T-Antigen G-Quadruplex DNA Helicase Inhibition by G-Quadruplex DNA-Interactive Agents. *Biochemistry*, **2008,** *47,* 1896-1909.

24. Pawsey, S.; Yach, K.; Reven, L. Self-Assembly of Carboxyalkylphosphonic Acids on Metal Oxide Powders. *Langmuir* **2002**, *18*, 5205-5212.

25. Pan, Y.; Tsai, H., G.; Jiang, J.; Kao, C.; Sung, T.; Chiu, P.; Saikia, D.; Chang, J.; Kao, H. Probing the Nature and Local Structure of Phosphonic Acid Groups in Mesoporous Silica SBA-15. *J. Phys. Chem. C* **2012**, *116*, 1658-1669.

26. Gomes, R.; Hassinen, A.; Szczygiel, A.; Zhao, Q.; Vantomme, A.; Martins, J., C.; Hens, Z. Binding of Phosphonic Acids to CdSe Quantum Dots: A Solution NMR Study. *J. Chem. Phys. Lett.* **2011**, *2,* 145-152.